The Realisation of Virtual Fluid Rendering on a Treadmill-Based Lower Limb Exoskeleton with Lateral Degrees of Freedom

MSc Thesis

Bauke Schenkelaars

Delft University of Technology

TU Delft

The Realisation of Virtual Fluid Rendering on a Treadmill-Based Lower Limb Exoskeleton with Lateral Degrees of Freedom

by

Bauke Schenkelaars

In partial fulfilment of the requirements for the degree of:
Master of Science in Robotics
at the Delft University of Technology,
to be defended publicly on Thursday, January 22nd 2026, at 13:00

Student number:	4953762	
Project duration:	September 2024 – January 2026	
Thesis committee:	Dr. ir. Laura Marchal-Crespo,	TU Delft, chair, supervisor
	Dr. Beatrice Luciani,	TU Delft, daily supervisor
	Prof. dr. ir. Martijn Wisse	TU Delft, external committee member

Cover: Photo of a person walking in the exoskeleton

TU Delft

Acknowledgements

I am very grateful to my supervisors, Laura Marchal-Crespo, Katherine Poggensee, and Beatrice Luciani, for their unwavering guidance and support throughout this thesis project. Their insights, patience, and constructive feedback have been invaluable, and I would not have been able to achieve as much without their help. I would also like to extend those thanks to everyone else at the MLN lab for the welcoming and supportive working environment. A special thanks goes to Alex van den Berg for his help in getting me started with working on the exoskeleton, understanding its existing controllers, and troubleshooting whenever the robot decided to start acting up again. I would also like to thank Martijn Wisse for agreeing to take some time out of his busy schedule to join my graduation committee as an external member.

Finally, I want to extend heartfelt thanks to my family and friends for their constant love and support throughout my years of studying in Delft. I especially want to highlight my study friends from the bachelor's – Willemijn, Jelle, Timo, and Koen – who were there for me at a time when I needed it the most. With my graduation, we are all done with studying, so our time of doing study projects together has come to an end, but the friendships we made along the way are not going anywhere. I also want to acknowledge my fellow teammates from Delft Hyperloop. That year was a defining chapter of my life, one filled with successes, challenges, and lessons that have shaped me for the rest of my personal and engineering life.

Bauke Schenkelaars
Delft, January 2026

Statement on the use of AI

All ideas presented in this thesis are the author's and the author's only. However, generative AI tools, specifically OpenAI's GPT-4 and GPT-5, were used to refine the text here and there for the sake of clarity and conciseness. Additionally, in the process of writing code for this project, the same tools were used to assist in converting pseudo-code to MATLAB R2013b-compatible syntax and in identifying and resolving bugs.

Contents

Acknowledgements . . . **ii**
Nomenclature . . . **iv**
Abstract . . . **1**
1 Introduction . . . **1**
2 Aquatic Treadmill Walking Model . . . **3**
2.1 Virtual Leg Kinematics . . . 3
2.2 Virtual Leg Geometry . . . 4
2.3 Virtual Fluid Dynamics . . . 4
2.4 Inverse kinematics . . . 6
3 Model Validation in Simulation . . . **6**
3.1 Methods . . . 6
3.2 Phase 1: Comparison with the literature . . . 7
3.3 Phase 2: Scaling with speed and depth . . . 7
3.3.1 Double movement speed . . . 8
3.3.2 Knee-deep water . . . 8
3.4 Phase 3: Different fluids . . . 8
3.4.1 Waist-deep Olive Oil . . . 9
3.4.2 Waist-deep Honey . . . 9
3.4.3 Waist-deep Peanut Butter . . . 9
4 Implementation . . . **9**
5 Experimental Proof of Concept . . . **10**
5.1 Methods . . . 11
5.2 Results . . . 11
5.3 Discussion . . . 11
5.3.1 Perceived Realism . . . 11
5.3.2 Perceived forces . . . 12
5.3.3 Identification of fluid environments . . . 12
6 Conclusion . . . **12**
References . . . **13**
Appendix A: Virtual Leg Kinematics . . . **15**
Appendix B: Gait Cycle Time Estimation . . . **18**
Appendix C: Simulation Input Kinematics . . . **19**
Appendix D: Simulation Results - Graphs . . . **20**
Appendix E: Proportional Resistance Model . . . **23**
Appendix F: Exoskeleton Start-up Procedure . . . **25**
Appendix G: Experiment Protocol . . . **26**
Appendix H: Experiment Questionnaire . . . **29**
Appendix I: Questionnaire Results . . . **33**
I.1 Realism Scores . . . 33
I.2 Identification of the rendered fluids . . . 33
I.3 Perceived Forces . . . 34

Nomenclature

Abbreviations

Abbreviation	Meaning
DALYs	Disability Adjusted Life Years
DOF	Degree(s) of Freedom
fig.	Figure
BWS	Body Weight Support
3D	Three-dimensional
eq.	Equation
CFD	Computational fluid dynamics
PC / xPC	(External) personal computer
IMU	Integrated motion unit
GUI	Graphical user interface

List of Symbols

Scalar Variables

Scalar variable	Meaning
w_p	Pelvis width
L_t	Thigh length
L_s	Shank length
r_h	Hip radius
r_k	Knee radius
r_a	Anle radius
ρ	Fluid density
V	Volume
r	radius
h	Thickness
μ	Viscosity
A_f	Frontal area in the direction of flow
C_D	Drag coefficient
t	Time
Δt	Sampling time step
Re	Reynolds number
x	Ratio between the maximum value of a force/torque in a simulation and that from the baseline simulation

Vector Variables

Vector variable	Meaning
$\mathbf{F}_b$	Buoyancy force
$\mathbf{F}_d$	Drag force
$\mathbf{g}$	Gravity
$\mathbf{u}$	Velocity
$\mathbf{u}_{rel}$	Relative velocity with respect to the fluid flow
$\mathbf{u}_c$	Velocity of the volumetric centre point
$\mathbf{P}_c$	Position of the volumetric centre point
$\boldsymbol{\tau}_{j,i}$	Contribution of slice i to the joint torque in joint j
$\mathbf{r}_{i,j}$	Moment arm between the volumetric centre point of slice i to joint j
$\mathbf{F}_{b,i}$	Buoyancy force acting on slice i
$\mathbf{F}_{d,i}$	Drag force acting on slice i
$\boldsymbol{\tau}_{j,ideal}$	Ideal torque to be rendered in joint j
$\mathbf{F}_p$	Pelvis force
$\mathbf{F}_{P,ideal}$	Ideal force to be rendered at the pelvis
ω_j	Angular velocity of DOF j

Mathematical Operators

Operator	Meaning
$\|\|\mathbf{q}\|\|$	Magnitude of vector $\mathbf{q}$
$\mathbf{q}[t-N]$	Vector $\mathbf{q}$ evaluated N time samples ago
${}^{Q}T_{S}$	Homogeneous transformation from reference frame Q to reference frame S
$\sum_{i=1}^{N}$	Summation from $i=1$ to $i=N$
$\max\|q\|$	Absolute maximum of variable q
$A << B$	A is more than one order of magnitude smaller than B

Degrees of Freedom

Degrees of Freedom	Meaning
x_P	Forward position of the pelvis
y_p	Lateral position of the pelvis
z_p	Vertical position of the pelvis
θ_p	Pelvis yaw angle
ϕ_p	Pelvis roll angle
ψ_p	Pelvis pitch angle
$\phi_h l$	Left Hip abduction angle
$\phi_h r$	Right Hip abduction angle
$\theta_h l$	Left Hip Flexion angle
$\theta_h r$	Right Hip Flexion angle
$\theta_k l$	Left Knee Flexion angle
$\theta_k r$	Right Knee Flexion angle

Reference Frames

Primary Axes	Meaning
X_O, Y_O, Z_O	Primary axes of inertial frame O, centred at the rest position of the pelvis midpoint
X_P, Y_P, Z_P	Primary axes of pelvis frame P, centred at the pelvis midpoint
X_{Hl1}, Y_{Hl1}, Z_{Hl1}	Primary axes of intermediate left hip frame $Hl1$, centred at the left hip
X_{Hl2}, Y_{Hl2}, Z_{Hl2}	Primary axes of left hip frame $Hl2$, centred at the left hip
X_{Hr1}, Y_{Hr1}, Z_{Hr1}	Primary axes of intermediate right hip frame $Hr1$, centred at the right hip
X_{Hr2}, Y_{Hr2}, Z_{Hr2}	Primary axes of right hip frame $Hr2$, centred at the right hip
X_{Kl}, Y_{Kl}, Z_{Kl}	Primary axes of left knee frame Kl, centred at the left knee
X_{Kr}, Y_{Kr}, Z_{Kr}	Primary axes of right knee frame kr, centred at the right knee

The Realisation of Virtual Fluid Rendering on a Treadmill-Based Lower Limb Exoskeleton with Lateral Degrees of Freedom

Bauke Schenkelaars

Wednesday 14th January, 2026

Abstract

Conventional post-stroke gait rehabilitation is labour-intensive, often requiring multiple therapists for physical assistance. Both robotic and aquatic therapies have been proposed to address this: robots can reduce therapist workload and provide adaptable feedback, while aquatic environments offer apparent weight reduction, improved balance, and muscle strengthening. Virtual aquatic therapy combines both approaches by haptically rendering the fluid dynamics of virtual water. In addition to the sagittal degrees of freedom offered by existing implementations, the treadmill-based exoskeleton used in this study enables hip abduction and lateral pelvis movements. A physics-based fluid rendering model is developed to compute drag and buoyancy forces acting on virtual legs moving through fluids. To match the real-world setup, the model simulates treadmill walking rather than the conventional free walking and includes the additional axes of motion. Simulations confirm that the model's outputs are consistent with the literature and scale properly with movement speed, submersion depth and the type of fluid being rendered. Through a proof-of-concept experiment, the successful integration into the exoskeleton's control framework is validated, demonstrating the feasibility of rendering diverse fluid environments with this system.

Keywords: Haptics, Gait Rehabilitation, Aquatic Therapy, Virtual Reality, Fluid Dynamics

1 Introduction

With over twelve million cases worldwide each year, stroke is one of the leading causes of disability-adjusted life year loss (DALYs). Only half of all patients survive, and those that do are often left with serious motor impairments [1]. Gait impairment is one such motor impairment that can occur due to a stroke. These patients still have intact muscles, nerves, and joints, so they are physically still capable of walking. However, due to brain damage incurred from the stroke, they have to relearn how to control the gait motions properly. Gait rehabilitation therapy can assist in this relearning process.

Conventional gait rehabilitation therapy involves treadmill training with a supported body weight to relieve the loading of the joints [2]. This requires physical assistance from multiple therapists to both guide the patient's leg motions and help them maintain balance. Given the growing global shortage of healthcare professionals [3], which is projected to further grow in the years to come due to the ageing population, such a labour-intensive and physically demanding therapy might not be sustainable in the future. Therefore, there is a demand for alternative therapies with a reduced physical reliance on therapists.

Rehabilitation robots, such as exoskeletons, can be part of the solution. With a robot providing physical assistance, the role of the therapist shifts from being physically demanding to mostly operating and supervising the robot. This not only reduces the physical workload but could also require fewer therapists altogether, as less hands-on effort is needed for a similar therapy.

A rehabilitation exoskeleton can be used in multiple ways [4], depending on what the therapist believes is best for the patient. For effective motor learning, the challenge level of an exercise should match the patient's skill [5]. The exercise should be challenging enough to be engaging, yet not so difficult that success feels unattainable. For some patients, the optimal use of the robot is for guiding them through the motions required for gait, which can be achieved through a position-controlled approach where the robot follows a predefined path. For other patients, it is best if they produce the motions themselves, while the robot provides forces to help lift the leg, maintain balance, or correct when straying too far from a reference motion. These applications use an impedance-controlled approach, as the robot provides forces based on patient-driven kinematics. If an even higher challenge level is desired, the robot can also be used to disrupt the patient by either resisting certain motions to demand more muscle effort or through unpredictable perturbations to challenge the patient in maintaining balance.

Another alternative to conventional gait rehabilitation therapy is aquatic therapy. In aquatic therapy, patients are submerged in warm water up to their waist or chest, which offers several physiological benefits [6]. The warmth and hydrostatic pressure of the water increase blood flow to the muscles and reduce muscle stiffness. Additionally, the buoyancy serves as a natural body weight support, relieving the patient's joints and muscles by reducing the apparent weight of the legs and upper body. In waist-deep water, the apparent total body weight is reduced to approximately half of the actual weight, and in chest-deep water to a third [7]. This also means that less physical assistance is required from the therapists. Another benefit of Aquatic therapy compared to overland therapies is that underwater, it takes more effort from the patient to swing the leg forward due to

the viscous drag, resulting in muscle strengthening, especially in the knee extensor muscles [8].

Aquatic therapy can also be beneficial for improving balance. This improvement in the patient's balance is the result of a reduced fear of falling while submerged [8]. Due to viscous damping, the water naturally cushions a potential fall, reducing the risk of injury and giving the patient more time to correct their balance. This makes the patient more willing to take risks, thus allowing them to attempt more challenging balance exercises. This damping effect of the water also means that less physical effort is required from the therapist during regular aquatic gait exercises, as they no longer need to provide balance support.

Given the potential benefits of both robotic treadmill training and aquatic therapy, there are also ongoing developments to create a single solution that combines the best of both. One approach to achieve this is by creating a rehabilitation exoskeleton that can be used while submerged in water [9], enabling aquatic therapy with assistance from the robot. However, the development and use of such waterproof hardware is expensive, so this research follows a different approach: haptically rendering the fluid interaction forces from submerged gait on an existing rehabilitation exoskeleton to create an aquatic therapy simulator.

Not all aspects of aquatic therapy can be replicated this way, as, for instance, there is no hydrostatic pressure or warmth. However, this virtual fluid approach does provide an opportunity for people to experience walking through fluids other than just water, which would be infeasible in real life. By rendering a fluid with a higher density, a larger buoyancy force is realised, which can help a patient lift their legs beyond what water could ever do, while with a higher density or viscosity, a stronger viscous drag can be realised, further promoting muscle strengthening.

Using a rehabilitation exoskeleton to create a virtual aquatic therapy experience is not a new concept. Kong *et al.* [10] used the free-walking exoskeleton SUBAR [11] to provide a natural-feeling assistance and resistance by using a physics-based virtual buoyancy and drag model. The SUBAR exoskeleton has hip, knee, and ankle joints that are actuated in flexion-extension, attached to a moving base that rides along as the patient walks. They used this to render the effects of drag and buoyancy, which they computed using basic formulae. In free walking, the stance leg's foot is stationary. Therefore, the forces acting on each leg segment contribute only to the torque of each joint closer to the stance leg's foot. This work was replicated by Chang and Jeon [12] on the EXOWheel exoskeleton, which, like SUBAR, is a free-walking exoskeleton with a base that moves with the patient. It has joints at the hips and knees that are actuated in flexion-extension. They used the same fluid rendering model from Kong *et al.* [10], but used it to render different virtual fluid environments with varying densities, viscosities, and gravities. Ertop *et al.* [13] also used the same model as Kong *et al.* [10] to compute the joint torques from drag and buoyancy, but implemented it on a treadmill-based exoskeleton, RobotGait, with actuated joints in flexion-extension at the hips and knees.

In all this existing literature, the robots used to render drag and buoyancy only have degrees of freedom in flexion-extension. This means that only movements within the sagittal plane are possible. This limits their applicability. Balance exercises, for instance, require the patient to correct for unbalanced lateral movements, which they cannot do if lateral movements are constrained. This study aims to fill this gap by expanding the degrees of freedom in which fluid forces are rendered to include lateral components. The main research question of this thesis is therefore: Can physics-based fluid rendering with adaptable fluid properties be realised on an exoskeleton with actuated degrees of freedom in both sagittal and lateral directions?

The robot used in this study is shown in fig. 1 and is explained in detail in Luciani *et al.* [14]. It is a treadmill-based exoskeleton that has actuated joints at the pelvis, hips and knees. The pelvis module contains both an actuated lateral slider and a passive spring mechanism, which allows for small movements in 6 degrees of freedom [15]. Each hip joint can move in both flexion-extension and abduction-adduction, and is actuated by a pair of linear motors that move laterally along with the pelvis slider. These linear actuators actuate the hip joint via a closed-linkage mechanism, such that if both actuators extend together, the hip joint extends, and if one extends while the other retracts, the hip joint abducts or adducts. By combining the two movements, any combination of flexion-extension and abduction-adduction angles within the operating range of the linear actuators and linkage mechanism can be achieved. The knee joint of the exoskeleton moves in flexion-extension only and is actuated by a rotary motor via a spindle mechanism between the thigh and the shank. Each leg of the exoskeleton attaches to the user via three cuffs: one for the thigh, above the knee, and two for the shank, below the knee and above the ankle.

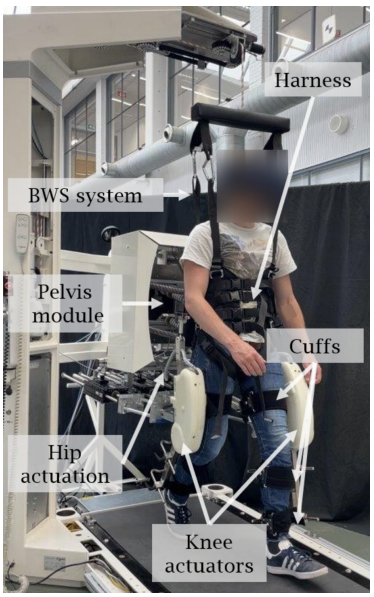

Figure 1: All the components of the exoskeleton system [14]

The aquatic treadmill walking model used to compute the fluid interaction forces that should be rendered at each joint is explained in section 2, followed in section 3 by the simulations that were run to validate the model. Section 4 describes how this model was implemented into the control architecture of the robot, after which section 5 demonstrates that this implementation was successful through a proof-of-concept pilot experiment. Lastly, conclusions are drawn in section 6.

2 Aquatic Treadmill Walking Model

The forces of drag and buoyancy that the exoskeleton should apply to the user in each joint are computed by a physics-based computational model. This model simulates a virtual environment where a virtual pair of legs walks on a treadmill while submerged up to a certain level in a virtual fluid. The model assumes that the maximum submersion depth is waist-depth, such that the drag and buoyancy acting on the trunk and upper body extremities can be ignored. The fluid in the environment is assumed to be either stationary or flowing at a constant speed.

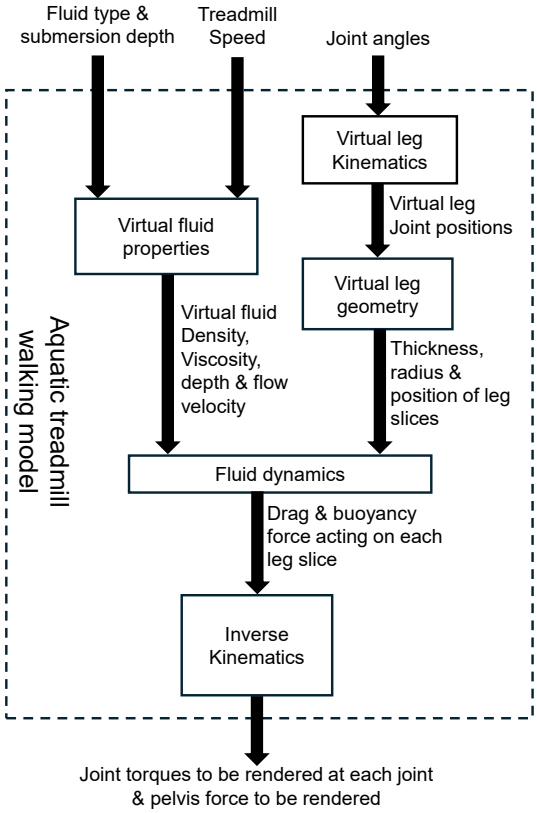

Figure 2: The model's computational pipeline

The computational pipeline of the model is illustrated in fig. 2 and can be divided into 4 steps that feed into each other:

1. The virtual leg kinematics step, which takes the joint angles acquired from the real-world exoskeleton and uses those to compute the pose of each joint of the virtual legs.
2. The virtual leg geometry step, which takes those poses and uses them to divide the virtual legs into a discrete set of cylindrical slices with each its own thickness, radius, and volumetric centre point.
3. The fluid dynamics step, which computes the drag and buoyancy force acting on each of those slices, based on the density, viscosity, depth, and flow velocity of the virtual fluid.
4. The inverse kinematics step, which computes the joint torque contributions and the lateral pelvis force contribution of each slice and adds those together for each joint to obtain the force or torque that the exoskeleton should render.

Each step is described in detail in its own subsection.

2.1 Virtual Leg Kinematics

The kinematics of the virtual legs in this model are based on treadmill walking instead of the free-walking kinematic model from Kong *et al.* [10]. The key difference between these kinematic models lies in the anchor point from which each leg segment's pose is defined. In free walking, the stance foot is semi-stationary between heel strike and toe-off, so the free-walking model uses the stance foot as its kinematic anchor, which switches over at each heel strike. On a treadmill, however, the stance leg moves backwards with the belt, while the pelvis is semi-stationary. Therefore, my aquatic treadmill walking model anchors the virtual legs at the pelvis midpoint, which can move laterally and vertically relative to the inertial frame.

The virtual legs are modelled as a multi-body system consisting of 5 rigid links that are connected in series at the joints. These 5 links represent the pelvis, 2 thighs, and 2 shanks. The feet are included in the rigid bodies of the shanks, as the exoskeleton does not have any attachments to the user's feet, so their pose is unknown. The multi-body system has 12 degrees of freedom, which follow from those of the exoskeleton:

- A 6 degrees of freedom pose of the pelvis (though, except for the lateral displacement, all of them are limited to small unactuated displacements and angles)
- Abduction-adduction and flexion-extension of the 2 hips
- Flexion-extension of the 2 knees

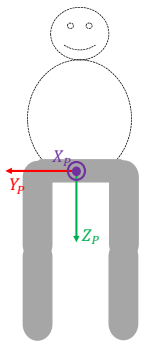

a) Pelvis frame P

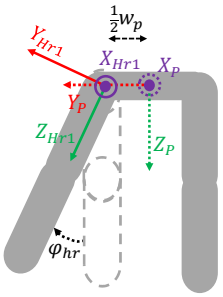

b) Intermediate right hip frame $Hr1$, defined by right hip abduction angle φ_{hr} and pelvis width w_p

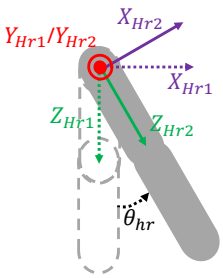

c) Right hip frame $Hr2$, defined by right hip flexion angle θ_{hr}

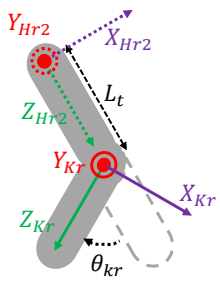

d) Right knee frame Kr, defined by right knee flexion angle θ_{kr} and thigh length L_t

Figure 3: Illustration of the position and orientation of the reference frames that represent the Cartesian pose of each virtual leg segment associated with the right leg. The frames for the left leg segments are equivalent, but mirrored with respect to the pelvis frame's XZ plane.

The 3D Cartesian pose of each of the 5 rigid links is defined by a reference frame centred at the joint where that link originates, and with one of its primary axes aligned with the link. For each hip, there is also an intermediate reference frame ($Hr1$ and $Hl1$) that only rotates with abduction-adduction, and not with flexion-extension. The position and orientation of all reference frames associated with the right leg are shown in fig. 3. The frames associated with the left leg are equivalent in definition, but mirrored with respect to the sagittal (XZ) plane of the pelvis frame. The position and orientation of these reference frames are computed through homogeneous transformations [16]. These transformations are worked out in detail in appendix A. In practice, the unactuated degrees of freedom of the pelvis are assumed to be 0 at the input of the model. This is done because no reliable sensor data for them is available on the robot, and they are limited to small displacements anyway.

2.2 Virtual Leg Geometry

With the pose of each leg segment defined, the next step is to apply some geometry to it. The forces acting on the trunk (including the pelvis) are neglected in this model, so the pelvis is modelled as an infinitely thin, frictionless rod of length w_p that connects the two hip joints. The geometries of the thigh and shank are approximated as truncated cones. Each segment has a fixed length. Thigh length L_t is measured from the hip joint to the knee joint, while shank length L_s is measured from the knee joint to the sole, as the foot is assumed to be part of the shank geometry. The radii of the truncated cones are defined at the joints through hip radius r_h, knee radius r_k, and ankle radius r_a. These dimensions are currently hard-coded in the model, using the values listed in table 1. However, in the future, they could be replaced by measurements of the user's real leg.

Table 1: The hard-coded dimensions used in the virtual leg geometry part of the model

Dimension	**Symbol**	**Length** (cm)
Pelvis width	w_p	30
Thigh length	L_t	44
Shank length	L_s	41
Radius at the hips	r_h	7
Radius at the knees	r_k	5
Radius at the ankles	r_a	3

To further simplify the virtual leg geometry, each conical leg segment is divided into 20 equally spaced discrete slices. Each slice is approximated as a cylinder with a fixed radius, which is obtained through linear interpolation between the radii of the joints at either end of the leg segment. The position of each slice is denoted by its volumetric centre point.

The feet are included in the leg geometry as a continuation of the shank cones. Although this is not a very accurate representation of the geometry, it is approximated as such for the sake of simplicity. This inaccuracy in the geometry definition is (partially) corrected for in the fluid dynamics part of the model by artificially increasing the drag and buoyancy acting on the slices that represent the feet.

2.3 Virtual Fluid Dynamics

The computed fluid dynamic forces are limited to drag and buoyancy. Other effects, such as lift or wave formation, are neglected because of their relatively small contributions and/or computational complexity. The directions in which the drag and buoyancy forces act are visualised in fig. 4. The drag and buoyancy are only computed for leg slices that are considered to be below the fluid surface, which is the case if the centre of volume of that slice is below the fluid's surface. As soon as the centre of volume is above the surface level, both the drag and buoyancy acting on that slice are assumed to be 0.

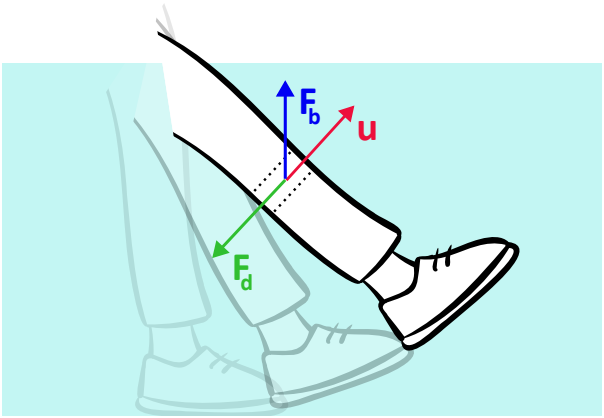

Figure 4: Directions of the forces of buoyancy ($\mathbf{F}_b$) and drag ($\mathbf{F}_b$) acting on one arbitrary leg slice (indicated by the black dashes). Magnitudes are not to scale. The buoyancy always points upwards (negative z-direction), and the direction of the drag is opposite to that of the velocity vector ($\mathbf{u}$).

The buoyancy and drag are computed using basic physics-based formulae. This makes it computationally very efficient, though it comes with the drawback that these formulae assume the fluid to be fully stationary or moving at a constant velocity. Any effects that moving through the fluid would have on the fluid itself, such as wave formation and induced flow [17], are neglected. There are other, more computationally complex, methods available that do keep track of the state of the fluid, such as a voxel grid method [18] or smoothed particle hydrodynamics [19], both of which are commonly used for haptic fluid rendering applications [20]. However, due to limitations in the computational hardware of the exoskeleton used in this research, these methods were not considered for this project.

The formula used to compute the buoyancy is given in eq. (1) [21]. The gravity $\mathbf{g}$ is constant for all slices, with a magnitude of $9.81\ \mathrm{m\,s^{-2}}$ in the positive z-direction, which ensures that the buoyancy always points upwards.

$$\mathbf{F}_b = -\rho V \mathbf{g} \tag{1}$$

The volume V is different for every slice of the legs, as it depends both on the slice's thickness h and radius r, as given by eq. (2).

$$V = \pi r^2 h \tag{2}$$

The density ρ depends on the fluid which is being rendered. Four fluids were implemented in this model. These fluids and their density and viscosity are listed in table 2.

Table 2: The four fluids implemented in this model, together with their density and viscosity, adapted from Chang and Jeon [12]

Fluid	**Density** ρ ($\mathrm{kg\,m^{-3}}$)	**Viscosity** μ (Pa s)
Water	1000	10^{-3}
Olive Oil	800	0.1
Honey	1420	5
Peanut Butter	1283	250

The formula used to compute the drag is shown in eq. (3) [21].

$$\mathbf{F}_d = -\frac{1}{2}\rho C_D A_f \|\mathbf{u}_{rel}\| \mathbf{u}_{rel} \tag{3}$$

In this equation, the relative velocity term $\mathbf{u}_{rel}$ is the velocity of the moving object relative to the velocity of the fluid. In this case, the moving object is the leg slice. By using the formula in eq. (3), it is assumed that every point within a slice has the same velocity as the centre point of that slice. The fourth-order backward finite difference formula in eq. (4) is used to estimate the velocity (u_c) of the slices' centre points, using their positions (P_c) in the past four time steps. The flow velocity of the virtual fluid is then subtracted from this estimated slice velocity to obtain the relative velocity term in eq. (3).

$$\mathbf{u}_c[t] = \frac{1}{\Delta t}\left(\frac{11}{6}\mathbf{P}_c[t] - 3\mathbf{P}_c[t-1] + \frac{3}{2}\mathbf{P}_c[t-2] - \frac{1}{3}\mathbf{P}_c[t-3]\right) \tag{4}$$

Since discrete velocity estimates are always sensitive to noise, even when using more than two time steps, a discrete low-pass filter is added to smooth the velocity estimates of all slices further. The final transfer function used in this filter is given by eq. (5). The cut-off frequency of this filter is 8.23 Hz, low enough to filter out any high-frequency noise, and still an order of magnitude above the expected gait cycle frequency, so the real velocity changes should be mostly unaffected.

$$H(z) = \frac{0.05z^{-1}}{1 - 0.95z^{-1}} \tag{5}$$

The area term A in eq. (3) ideally depends on the leg slice's surface area orthogonal to the relative velocity, but in this model, this velocity dependence is neglected. Each slice is a short cylindrical section of a longer leg segment, and only has its radial outer surface exposed to the fluid. During normal gait, the movements of each leg segment approximate those of a pendulum, so the velocity has negligible axial components. Consequently, the velocity's direction should primarily be in a radial direction. Thus, A is taken as the radial projection of the outer surface, which depends only on the slice radius r and thickness h, as denoted by eq. (6).

$$A_f = 2r \cdot h \tag{6}$$

The last term in eq. (3) to be computed is the drag coefficient C_D. This is a complicated term that depends on both the shape of the object and the level of turbulence in the flow. Because of this complexity, drag coefficients are often determined empirically. Since each leg slice has been simplified to be cylindrical, existing empirical data on smooth near-infinite cylinders can be used to estimate the drag coefficients for this model. The fit curve in fig. 5, constructed from data obtained in three different flow domains by Jayaweera and Mason [22], Tritton [23], and Wieselsberger [24], is logarithmically interpolated to estimate the drag coefficient when the Reynolds number (Re) is known.

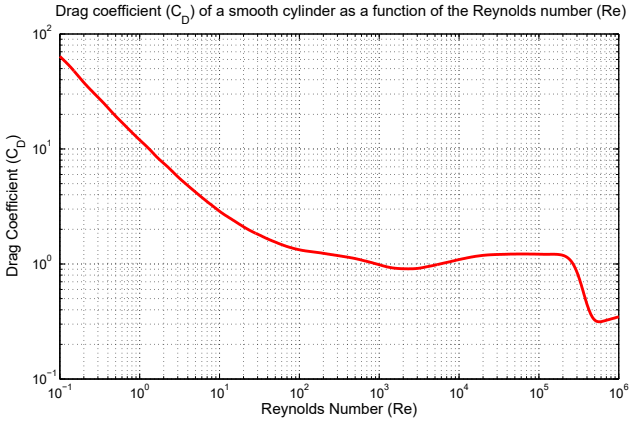

Figure 5: Fit curve of the drag coefficient of a cylinder as a function of the Reynolds number, based on data from Jayaweera and Mason [22], Tritton [23], and Wieselsberger [24]

The Reynolds number is computed using eq. (7) [21], using the relative velocity, slice radius, fluid density and the fluid viscosity μ, as listed in table 2.

$$Re = 2\frac{\rho r}{\mu}\|\mathbf{u}_{rel}\| \tag{7}$$

In the geometry of the leg, the feet are included as a continuation of the shank. However, the shape and volume of a foot are very different from those of the rest of the shank. Therefore, the fluid dynamic forces acting on the lowest three cylindrical slices of each shank are artificially increased to better represent the presence of the foot. The length of the foot is roughly 3 times the radius of the ankle, so it is assumed that these bottom three slices occupy 3 times as much volume as they would if they were a continuation of the shank. Therefore, the buoyancy force acting on those slices is increased by a factor of 3.

For the drag, the feet are assumed to be constantly in the anatomical reference pose. As shown by Akiyama *et al.* [25], in reality, the foot is in plantar flexion during toe-off and only in the reference pose in the middle of the swing phase. However, since the velocity of the foot is the highest during swing, this is the pose that is used when determining the correction factor for the drag acting on the feet. Lauer [26] computed the drag coefficient of both the foot and shank through computational fluid dynamics (CFD) simulations. He showed that for a forward swing, the drag coefficient of the foot is about 30% of that of the shank. When the shank and foot are attached, the water that flows around the foot also flows around the shank afterwards,

as it would otherwise get trapped near the ankle. Therefore, the assumption is made that the presence of the foot increases the drag in the bottom three shank slices by 30%.

2.4 Inverse kinematics

The total force exerted on a single leg slice is the sum of its drag and buoyancy force. To compute the contribution of a specific slice i to joint torque $\boldsymbol{\tau}_{j,i}$ of joint j, the total force of slice i is multiplied by the moment arm from the centre point of the slice to the joint ($\mathbf{r}_{i,j}$), as shown in eq. (8). Since the pelvis is considered the semi-stationary anchoring point of the body in the treadmill walking model, the only torque contributions that are computed are those where the joint is between the leg slice and the pelvis. So the forces acting on a thigh slice only contribute to the hip torque of that leg, while the forces acting on a shank slice contribute to both the knee and hip joint of that leg.

$$\boldsymbol{\tau}_{j,i} = \mathbf{r}_{i,j} \times (\mathbf{F}_{b,i} + \mathbf{F}_{d,i}) \tag{8}$$

Ideally, the joint torque τ_j that the exoskeleton produces in joint j is then the sum of all torque contributions from the N slices that contribute to it, as shown in eq. (9).

$$\boldsymbol{\tau}_{j,ideal} = \sum_{i=1}^{N} \boldsymbol{\tau}_{j,i} \tag{9}$$

However, this ideal torque vector has three Cartesian components, while the actual joints of the exoskeleton have only one (for the knee) or two (for the hips) axes of actuation. Therefore, all the torque components that can not be actuated need to be discarded. The ideal torque computed in eq. (9) is defined in the global inertial reference frame. Using the rotation-matrix component of the homogeneous transformations computed earlier, the torque is transformed to the local reference frame of the joint on which the torque should act. This is needed because only in the local reference frame is it defined which torque components can be actuated. For the knees, that is only the y-component of the torque (flexion-extension), and for the hips, both the x- and y-components (abduction-adduction, and flexion-extension, respectively). The other components are discarded.

The exoskeleton used in this study can also apply lateral force perturbations to the pelvis. The total force acting on the pelvis ($\mathbf{F}_P$) under the semi-stationary assumption is the sum of all the forces acting on all 80 leg slices, as shown in eq. (10). Once again, this is merely the ideal pelvis force vector as it has three Cartesian components, while the pelvis can only be actuated laterally, in the y-direction. Therefore, the x-and z-components are once again discarded. It can be noted that since the buoyancy forces all act in the negative z-direction, and the z-component of the pelvis force is discarded, the buoyancy does not contribute to the actual rendered pelvis force.

$$\mathbf{F}_{P,ideal} = \sum_{i=1}^{80} \mathbf{F}_{b,i} + \sum_{i=1}^{80} \mathbf{F}_{d,i} \tag{10}$$

3 Model Validation in Simulation

3.1 Methods

The model's ability to compute the buoyancy and drag contributions to each joint torque and force is validated through simulations. This done in three phases:

1. Directly comparing results to the literature
2. Checking the scaling with speed and submersion depth
3. Verifying the ability to render different fluids

Phase 1 uses kinematic motion-captured data from Akiyama *et al.* [25] of walking at 0.31 $\mathrm{m\,s^{-1}}$ in chest-deep water, enabling a direct comparison with results from their model based on the swimming simulator SWUM [27]. However, Akiyama's data does not include hip abduction and lateral pelvis displacements. Therefore, simulation phases 2 and 3 are run using kinematic input data from Woernle [28], who extended the gait database by Fukuchi *et al.* [29] to include lateral pelvis displacements. By averaging the extended data from the three lowest walking speeds of each participant in the database, he created a standard kinematic gait pattern for walking in the exoskeleton used in this study. It should be noted that this standard gait pattern is for walking on land. As people walking through real water show slightly different kinematics compared to overland walking [30–32], the same can likely be observed for haptic water rendering.

The kinematic data from both sources are extracted from graphs. Using PlotDigitizer [33], the graphs are sampled at 100 samples per gait cycle. The extracted data is then subsampled to a frequency of 1 kHz to match the operating frequency of the robot, using piecewise cubic Hermite interpolation. The number of samples required for this depends on the period of one gait cycle. The gait cycle time for walking at a speed of 0.31 $\mathrm{m\,s^{-1}}$ is estimated using a power law fit through the data from Fukuchi *et al.* [29], which is visualised in appendix B. The subsampled data is extended to three gait cycles, after which a smoothing filter is applied to ensure smooth (angular) velocities. Although each simulation is run for three gait cycles, only the second cycle is analysed to prevent transient smoothing effects influencing the results. The resulting kinematic inputs are shown in appendix C.

As no ground truth output exists for simulations with the kinematics of Woernle [28], phase 2 instead applies scaling laws to make a hypothesis on how drag and buoyancy should scale with the movement speed and submersion depth. These hypotheses are tested by comparing simulations with those parameters changed to a baseline simulation of walking through waist-deep water at 0.31 $\mathrm{m\,s^{-1}}$. Simulation phase 3 uses the same baseline simulation to analyse the effects of rendering olive oil, honey, and peanut butter, instead of water. Here, these effects are compared to literature results from Chang and Jeon [12], who ran simulations of the same fluids with their submerged walking model. In both phases, the results are quantified by scaling factors x, representing the ratio between the peak drag or buoyancy component of a joint to that in the baseline, as in eq. (11).

$$x = \frac{\max|\tau|}{\max|\tau_{baseline}|} \tag{11}$$

Since the model is compared to literature results on free walk-

ing, it too should simulate free walking. Therefore, to convert treadmill walking into an estimate of free walking, the fluids are simulated as flowing with the same velocity as the treadmill. This trick works because in treadmill walking, the pelvis is stationary relative to the fluid while the stance leg moves, whereas in free walking, the opposite is true. Therefore, matching the fluid velocity to the stance leg approximates free walking.

3.2 Phase 1: Comparison with the literature

A comparison between the simulated hip and knee flexion torques from my aquatic treadmill walking model and those reported by Akiyama *et al.* [25] is shown in fig. 6. For the knee, the results align closely: both torque profiles exhibit a similar shape, and the peak torque in my simulation is only 7% lower. For the hip, however, the results only match during stance (0–60%) and late swing (90–100%), whereas the results diverge substantially during mid-swing, where the peak torques occur.

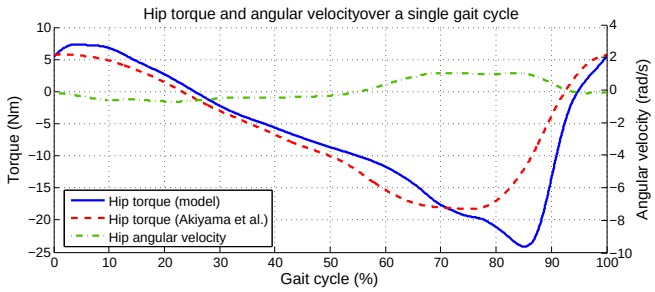

a) Hip flexion torque and angular velocity

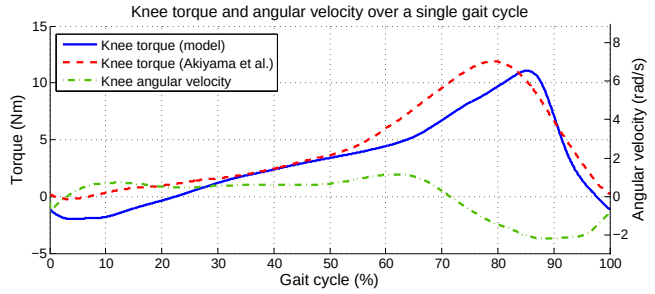

b) Knee flexion torque and angular velocity

Figure 6: The total fluid torques from my model compared to those of Akiyama *et al.* [25], as well as the angular velocity of both joints.

In Akiyama's simulation, the hip torque plateaus between 65–80% of the gait cycle. In contrast, my simulation only shows a brief plateau at 75%, followed by a continued rise to a torque peak at 85% of the cycle. This torque peak has a 32% higher magnitude than the plateau level of Akiyama. A similar but smaller delay in peak timing is also observed for the knee torque, suggesting a difference in the computed fluid forces acting on the shank and foot.

Between 50–65% of the gait cycle, the shank accelerates forward as the hip accelerates in flexion, while knee flexion partially counteracts this. From 65–85%, the hip angular velocity remains constant, but the knee starts accelerating in extension, thus further increasing the shank velocity. Only after 85% of the cycle, when the hip decelerates and the knee velocity plateaus, does the shank decelerate. Thus, the shank velocity, and consequently the drag force acting on it, peaks around 85% of the gait cycle, consistent with the timing of my simulated maximum torques. This supports the validity of my model over theirs.

The observed differences cannot be attributed to the ankle movements that are neglected in my model. Instead of the assumed fixed angle of 0°, Akiyama's motion-captured data show up to 80°of plantar flexion. At 85% of the gait cycle, where my simulated torques peak, the real plantar flexion of the ankle was 40°. This would increase the frontal area and drag coefficient of the foot compared to the assumed 0°. Therefore, if the unmodelled ankle pose had caused these discrepancies, the torques would have been underestimated, not overestimated.

3.3 Phase 2: Scaling with speed and depth

Figure 7 shows the results of walking at $0.31\,\mathrm{m\,s^{-1}}$ through waist-deep water, with Woernle's Kinematics. This is the baseline against which the remaining simulations will be compared.

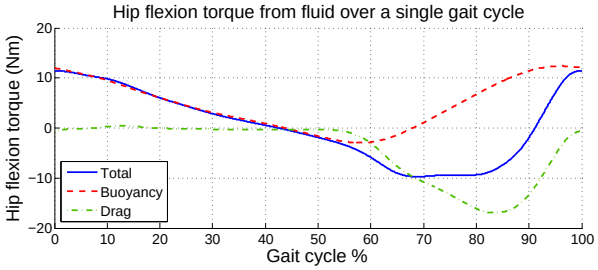

a) Hip flexion torques

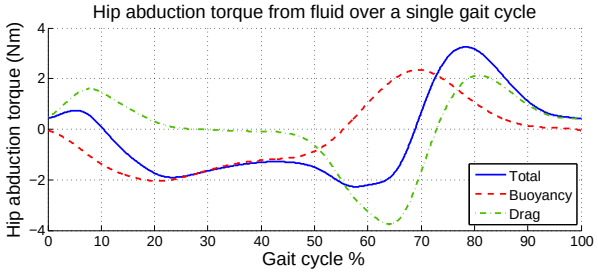

b) Hip abduction torques

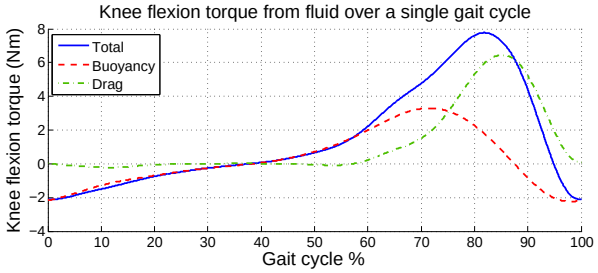

c) Knee flexion torques

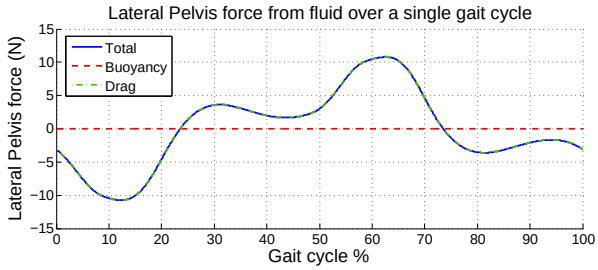

d) Lateral pelvis forces

Figure 7: Baseline simulation results for waist-deep water using the kinematics from Woernle [28].

3.3.1 Double movement speed

The next simulation uses the same kinematics and the same virtual fluid environment of waist-deep water. However, what is different is that the speed of all the movements is doubled. This means two things: the walking speed is increased to 0.62 $m\,s^{-1}$ and the gait cycle time is reduced to 1.08 s. This is not intended as an accurate representation of walking twice as fast. When a person walks faster, their stride length typically increases. Therefore, the relation between walking speed and gait cycle time is non-linear, as shown in appendix B. Instead, this simulation represents a scenario where a person makes the exact same kinematic movements in half the time by moving their limbs twice as fast.

The reason for this approach is that the effect of the double movement speed would be much harder to predict if it were paired with a change in stride length. On the other hand, with every movement doubled, the relative velocity between the limb and the fluid doubles as well. This should not affect the buoyancy, as buoyancy is a hydrostatic effect. The drag, however, should increase by a factor of 4, due to the quadratic relation between relative velocity and drag.

The resulting graphs of this simulation are shown in fig. 15 in appendix D. Table 3 shows the factors by which the peak torque components increased in this simulation compared to the baseline. As expected, the buoyancy is almost unchanged. The small changes that are observed can be attributed to the reduced number of simulation steps per gait cycle, as the simulation is run at the same sampling frequency but with a reduced gait cycle time. The drag contributions increased by almost a factor of 4, which also matches the hypothesis. Therefore, this simulation shows that the model scales properly with varying movement speeds.

Table 3: The peak value of each torque component and the total torque in the double speed simulation to the peak torques in the baseline simulation (multiplier x in eq. (11)).

	Drag	Buoyancy	total
Hip flexion torque	3.91	0.99	5.01
Hip abduction torque	3.67	0.97	3.70
Knee flexion torque	3.90	0.99	3.33
Lateral pelvis force	3.88	-	3.88

3.3.2 Knee-deep water

The next simulation is done at the original walking speed (0.31 $m\,s^{-1}$), but this time, the water level is only knee-deep instead of waist-deep. This means that the thigh will remain fully above the fluid surface throughout the gait cycle, so only the forces acting on the shank will continue to contribute. This should have almost no impact on the knee torques, as they are only influenced by the shank forces regardless of whether the thigh is submerged. The hip and pelvis, however, are usually influenced by both the shank and the thigh, of which only the former remains. Therefore, the amount by which the drag and buoyancy will decrease depends on how much the thigh contributes compared to the shank.

The thigh has a larger volume than the shank due to its larger radius, but the moment arm from the shank to the hip is much longer than that from the thigh to the hip. With those two effects combined, they both contribute a similar amount to the buoyancy torque of the hip, so the buoyancy should be roughly halved when the submersion depth is reduced to knee-level.

The experienced drag torque at the hip, on the other hand, is much more dominated by the shank. The velocity of each leg slice scales linearly with the angular velocity of the hip and the moment arm between the hip and that leg slice. The drag force exerted on that leg slice scales with the velocity squared and thus also with the moment arm squared. If you then compute the contribution of that force to the experienced hip torque, this requires another multiplication by the moment arm. Overall, the drag torque experienced at the hip therefore scales with the moment arm cubed. Since the moment arms of the shank are much longer than those of the thigh, a reduced submersion depth will only slightly reduce the experienced drag at the hips.

The resulting graphs of this simulation are shown in fig. 16 in appendix D. Table 4 shows the factors by which the peak torque components increased in this simulation compared to the baseline. As expected, the knee torques are the same as in the baseline. For the hip, the buoyancy torques were reduced by 46% and 39% for flexion-extension and abduction-adduction, respectively. This matches the hypothesis that the buoyancy torque would be roughly halved. The drag torque at the hips reduced by 11% and 27%, which is, as expected, a much smaller reduction than that of the buoyancy. This shows that the model is valid for varying submersion depths.

Table 4: The peak value of each torque component and the total torque in the knee-deep water simulation to the peak torques in the baseline simulation (multiplier x in eq. (11)).

	Drag	Buoyancy	total
Hip flexion torque	0.89	0.54	1.03
Hip abduction torque	0.73	0.61	0.77
Knee flexion torque	1.00	1.00	0.99
Lateral pelvis force	0.53	-	0.53

It should be noted that the graphs of the hip and knee torques in fig. 16 show a couple of small jumps. These jumps are the result of the centre of volume of one of the highest shank slices clipping through the surface level. As the model does not consider the partial submersion of a slice, when the centre point clips through the fluid surface, it suddenly starts or stops contributing within the span of a single time step. The magnitudes of these jumps are up to 0.3 Nm for the hip flexion, 0.03 for the knee flexion, and 0.07 for hip abduction. As the magnitudes of these jumps are more than a full order of magnitude smaller than the torque magnitude, they will likely be difficult to notice in practice.

3.4 Phase 3: Different fluids

In this simulation phase, three simulations are run with different virtual fluid properties. The fluid properties that are varied are the density and viscosity. The fluids simulated this way are olive oil, honey, and peanut butter, whose fluid properties are listed in table 2. Each simulation is run at a speed of 0.31 $m\,s^{-1}$ with waist-deep submersion. The results of those simulations

are compared against the baseline simulation of waist-deep water from the previous simulation phase. Chang and Jeon [12] have done the same thing using their model, enabling a direct comparison with their results. Chang and Jeon only included hip flexion and knee flexion in their model, so the other degrees of freedom cannot be compared. The factors by which the peak torque contributions of drag and buoyancy increased in their simulations compared to their water baseline are listed in table 5. According to their results, the factors for the hip and knee were the same, hence why they are only reported once.

Table 5: The hip and knee torque components simulated by Chang and Jeon [12] relative to those from their water simulation. The values shown are equivalent to the multiplier x in eq. (11).

	Drag	Buoyancy
Olive Oil	0.67	0.80
Honey	2.22	1.42
Peanut Butter	16.49	1.28

3.4.1 Waist-deep Olive Oil

The resulting graphs for the simulation with olive oil are shown in fig. 17 in appendix D. The peak torque multipliers of each joint are listed in table 6. For both the knee and hip flexion, the buoyancy decreased by 20%, perfectly matching the results from Chang and Jeon. The decrease in drag of 31% for both joints is also very similar to Chang and Jeon's results, as the difference is just 2 percentage points. This shows that the model works well for olive oil as its virtual fluid.

Table 6: The peak value of each torque component and the total torque in the waist-deep olive oil simulation relative to the peak torques in the baseline simulation (multiplier x in eq. (11)).

	Drag	Buoyancy	total
Hip flexion torque	0.69	0.80	0.80
Hip abduction torque	0.74	0.80	0.74
Knee flexion torque	0.69	0.80	0.72
Lateral pelvis force	0.76	-	0.76

3.4.2 Waist-deep Honey

Next, a simulation is run for honey, of which the results graphs are shown in fig. 18 in appendix D. The peak torque multipliers of each joint are listed in table 7. Again, with a 42% increase, the buoyancy torques of both hip and knee flexion match perfectly with those of Chang and Jeon. Likewise, the knee flexion drag increasing by a factor of 2.22 is the same result as they have. The hip flexion drag increases by a factor of 2.29, 7 percentage points more than for Chang and Jeon. Proportionally, this is only a 3% difference, which shows that the model is also suitable for simulating honey.

Table 7: The peak value of each torque component and the total torque in the waist-deep honey simulation relative to the peak torques in the baseline simulation (multiplier x in eq. (11)).

	Drag	Buoyancy	total
Hip flexion torque	2.29	1.42	2.44
Hip abduction torque	2.81	1.42	2.7
Knee flexion torque	2.22	1.42	2.05
Lateral pelvis force	3.16	-	3.16

3.4.3 Waist-deep Peanut Butter

Lastly, a simulation is run for waist-deep peanut butter, the output graphs of which are shown in fig. 19 in appendix D. The peak torque multipliers of each joint are listed in table 8. Again, the buoyancy increase by 28% matches perfectly with the results from Chang and Jeon. However, the drag increases much more than what they reported. The increase factors of 22.80 and 21.32 are more than 30% higher than their 16.49.

Table 8: The peak value of each torque component and the total torque in the waist-deep peanut butter simulation relative to the peak torques in the baseline simulation (multiplier x in eq. (11)).

	Drag	Buoyancy	total
Hip flexion torque	22.80	1.28	32.84
Hip abduction torque	33.63	1.28	38.41
Knee flexion torque	21.32	1.28	17.81
Lateral pelvis force	40.26	-	40.26

This difference is not entirely surprising. Peanut butter has such a high viscosity that the fluid flow is in the domain of creeping flow (Re « 1) [21]. Within this domain, the drag coefficient decreases logarithmically with the Reynolds number. This means that even a proportionally small change in velocity can cause a proportionally large change in experienced drag. Chang and Jeon did not report their input kinematics nor their simulated walking speed. It is therefore very likely that their simulated legs are moving at a slightly different velocity than those in my simulation. For comparing water, olive oil, and honey, this difference in movement speed does not influence the results much, as their lower viscosities result in laminar or turbulent flow. In those flow domains, the drag coefficient is much less dependent on the Reynolds number, so a small change in velocity has a proportionally much smaller effect on the experienced drag. Since peanut butter is viscous enough to result in creeping flow, any difference in velocity would have a big impact on the experienced drag, which explains the difference between our results

This means that it cannot be said with certainty how well the model can render peanut butter. Because of this, and the fact that the simulated torques are a full order of magnitude higher than those of the other fluids, it is decided that the rendering of peanut butter will not be used in practice on the robot.

4 Implementation

The aquatic treadmill model is built in Simulink in MATLAB R2013b [34] to be compliant with the exoskeleton's existing control architecture, which utilises the xPC target library. The Simulink controller model of the robot runs on the external PC (xPC). Via a UDP connection over Ethernet, commands are sent from a host PC to the xPC. The xPC processes the sensor data, runs the controller and sends commands to the motor drives.

The exoskeleton has rotary encoders in the two knee joints and linear encoders in the four linear motors that actuate the hips and the linear actuator of the pelvis. The linear encoder data for the hips is processed through a forward kinematic model of the linkage mechanism between the actuators and the thigh [14] to estimate the abduction and flexion angles of the hips. The

linear encoder data from the pelvis can be used directly as an estimate for the lateral pelvis position. The pelvis module also includes an IMU and an infrared motion camera to estimate the pose of the pelvis backplate. However, since the spring mechanism only allows for small displacements, this sensor data is not used. Instead, all degrees of freedom of the pelvis other than the lateral position of the pelvis slider are assumed to be 0.

The rotary encoder data of the knees can also be used directly for estimating the knee flexion angle. However, as the encoder has its rollover point within the operational limits of the joint, this would sometimes result in an erroneously high angular velocity estimate, causing the robot to throw an error. This happens because the encoder angle suddenly jumps from 0°to 360°, or vice versa, within a single computation step, which the velocity estimator would interpret as a full rotation in only 1 ms. To circumvent this issue, the knee encoder data now gets remapped to a range of ±180°, where 0°is when the shank is in-line with the thigh. This way, the remapped angle rolls over at 180°, which is well outside the physical limits of the joints.

These estimates for the hip and knee angles and the lateral pelvis position are fed to the aquatic treadmill walking model as the kinematic input. However, the model has 3 more inputs:

1. The fluid type to be rendered (Water, Olive oil, or Honey)
2. The submersion depth (No submersion, Knee-deep submersion, or Waist-deep submersion)
3. The flow velocity of the fluid

A graphical user interface (GUI) was created to set the type of fluid and the submersion depth from the host PC, which are then fed as inputs to the model. The flow velocity has two modes: no flow or counterflow. In counterflow mode, the fluid flows with the speed of the treadmill to approximate the interaction forces for free walking as opposed to the usual treadmill walking. Counterflow mode can be enabled and disabled in the same GUI in which the fluid parameters are set. The fluid rendering GUI has three more toggle switches:

1. Enable/disable data logging
2. Enable/disable the rendering of buoyancy
3. Enable/disable the fluid rendering altogether

In the fluid rendering GUI, it can also be selected which fluid rendering model should be used. The default model is the aquatic treadmill walking model described in section 2, but it is also possible to switch to a simpler proportional resistance model. This model was implemented as a baseline against which the aquatic treadmill walking model can be compared during an experiment. An explanation of how this proportional resistance model works can be found in appendix E.

With the kinematic inputs extracted from the encoders and the rendering parameters set via the GUI, the model can compute the joint torques and forces required to render the fluid environment. However, the exoskeleton is position-controlled, not force-controlled, so these torques and forces cannot directly be converted to motor demands. Instead, it first needs to be estimated for what (angular) displacements the robot would produce the demanded torques and forces. Accurately making those estimates requires an inverse dynamics model of the exoskeleton and its user combined. Unfortunately, it would be impossible to create an individual inverse dynamics model for every single user. The best feasible option would be to create an inverse dynamics model based on a reference person and then scale it to the user's length and weight. However, although I would recommend deriving and implementing such an inverse dynamics model in future work, it does not yet exist at the time of this writing.

Instead, the assumption is made that the relation between (angular) displacement and force or torque is linear and independent of the current joint poses. In practice, these assumptions might not be entirely valid, but without a detailed inverse dynamics model, this is the closest feasible approximation. Therefore, the torque and force demands from the model are multiplied by constant linear gains to estimate the desired (angular) displacements. For each degree of freedom, these desired displacements are combined with the current positions and angles to get the target pose of each joint. These target poses are then fed to an inverse kinematic model of the robot to compute the reference positions and angles of all motors.

In parallel, a transparency controller estimates the forces of gravity acting on the robot and the resistance in the actuators and joints. Based on those estimates, it outputs a counteracting motor reference correction, which is added to the motor reference from the haptic rendering. This way, the effects of gravity and friction are mostly eliminated from the robot, resulting in a much more transparent rendering of the fluid environment.

When necessary, the motor references are further adjusted by soft-stop controllers, which are implemented to prevent the robot from hitting any physical limits. For the knees and pelvis, they act as virtual spring-dampers that engage when a joint is closer to its end stop than a predefined threshold. The soft-stop controller for the hip joints does the same thing for each of the four linear actuators, while also limiting the relative difference between two coupled actuators to prevent their coupling mechanism from exceeding its physical limits. To prevent the virtual spring-dampers of the soft-stop controllers from being overpowered by the motor demands from the haptic rendering, a dynamic saturation is implemented, which limits the haptic motor demands based on each actuator's distance to its end stop. When this distance is less than twice the soft-stop engagement threshold, and the commanded motion would further reduce it, the haptic motor demand is linearly attenuated, such that it reaches zero when the soft-stop engages.

After the soft-stop corrections are applied, the resulting motor demands are sent to the motor drives. This whole process runs on the target xPC at an operating frequency of 1 kHz. The start-up procedure for turning on the fluid rendering on the exoskeleton is listed in appendix F.

5 Experimental Proof of Concept

A pilot experiment was conducted as a proof of concept for implementing the aquatic treadmill walking model on the exoskeleton. The setup was designed to be scalable to a larger study

that will evaluate the perceived realism of the model, compared to a simpler proportional resistance model. In addition, the experiment examines how the perceived forces and torques vary between fluid environments and assesses the extent to which users can identify these environments by feel.

5.1 Methods

The experiment consists of 20 trials for each participant, split up into 4 blocks of 5 trials each. Each block uses a different model to render the fluids, as detailed in table 9. The order in which the four models are used is randomised. The aquatic treadmill walking model is used in three different modes. The rendering mode without buoyancy or counterflow renders only viscous drag, similarly to the proportional resistance model. The rendering mode with buoyancy, but without counterflow, is the default operating mode where the virtual avatar walks on a submerged treadmill. The rendering mode with counterflow represents a free walking virtual avatar, whose movement speed is represented by the fluid's counterflow.

Table 9: The four rendering models used in the experiment

	Rendering model
A	Proportional resistance model
B	Aquatic Treadmill Walking model, without buoyancy or counterflow
C	Aquatic Treadmill Walking model, with buoyancy, but without counterflow
D	Aquatic Treadmill Walking model, with buoyancy, and with counterflow

Each model has its own block of five trials, all of which have a different fluid environment that is being rendered. The five fluid environments that are rendered are listed in table 10 and appear in a random order for each block. When air is rendered, none of the models output any fluid forces, so it serves as a control condition that is the same for all rendering models.

Table 10: The 5 fluid environments that will be rendered in a random order for each block of the experiment

	Submersion level	Rendered fluid
1	No submersion	Air
2	Knee-deep	Water
3	Waist-deep	Water
4	Waist-deep	Honey
5	Waist-deep	Oil

The full experiment protocol can be found in appendix G. During each trial, the participant walks for 60 s on the treadmill at a speed of 1 $\mathrm{km\,h^{-1}}$, while the exoskeleton applies the fluid rendering forces to them. It is unknown to the participant which fluid environment is being rendered or which rendering model is used. Instead, they are tasked to identify the fluid environments by feel as they are walking. Before the first trial, there is a single familiarisation trial with the exoskeleton in transparency mode. This transparency mode is equivalent to the control condition of air rendering. The objective of this familiarisation trial is to familiarise the participant with the treadmill speed and the feeling of walking in the exoskeleton.

For each trial, the haptic outputs of the rendering model are recorded, along with the joint kinematics and the knee interaction torques between the participant and the robot. This data is recorded at the exoskeleton's operating frequency of 1 kHz.

After each trial, the participant is asked to fill in a questionnaire indicating if they perceived the treadmill speed as adequate, stating how realistic the fluid rendering felt (through the realism questions from the haptic experience inventory [35]), and how strong the perceived forces and torques were at the hips, knees, and pelvis (through a CR10 version of the Borg Rating of Perceived Exertion [36]). Additionally, after each block of 5 trials, they are asked to match each trial with the fluid environment they believed was being rendered, and to report the level of fatigue and discomfort they experienced (through questions based on the Improved Musculoskeletal Discomfort Assessment Tool [37]). The full questionnaire can be found in appendix H.

5.2 Results

The experiment is run with 3 healthy participants (1 Male, 2 Female, ages 28-45) with a mixed level of previous experience with the exoskeleton. All participants are staff of the Motor Learning and Neurorehabilitation lab at the Mechanical Engineering faculty of TU Delft, so ethical approval was not required. Due to technical malfunctions and changes in the experiment protocol, not all participants were able to have a single session with all four models. For participant 3, the blocks of trials were divided over two sessions. For participant 1, the aquatic treadmill walking model with buoyancy, but without counterflow, is not included at all. An overview of the questionnaire answers of the three participants is presented in appendix I.

5.3 Discussion

With only three participants in the pilot experiment, making statistically significant statements based on the experiment data is not feasible. However, it is still important to analyse the results to make observations that may indicate a significant effect or an issue with the methodology. These indications can then be used to refine the methodology for future research.

5.3.1 Perceived Realism

Looking at the total realism scores given by the participants (table 17), strong interpersonal biases become apparent. Given the inherently subjective nature of realism, such biases are to be expected. In a larger-scale study, the scores should be normalised per participant to eliminate these biases and enable meaningful statistical analysis across multiple participants. However, with only three participants and partially incomplete data, such an analysis would not yield statistically significant results and was therefore omitted.

There also seems to be an issue of low within-participant consistency. The control condition (air rendering) was identical across all models and should theoretically receive the same realism rating. In practice, however, scores for these air trials varied substantially even within a single participant. This inconsistency in scores for the same condition indicates that participants might score the realism comparatively to the trials around it, or that there is a certain level of randomness to each given score.

Part of this randomness may originate from the questionnaire design. The four realism-related questions were reportedly very similar, and participants had difficulty distinguishing between them. In the original Haptic Experience Inventory (HXI) [35], these questions are randomly mixed in with questions related to other perceptual dimensions, which makes their similarity less apparent. Grouping these questions together in the questionnaire might have reduced their validity.

Another factor influencing the scores is the lack of a ground-truth reference. Participants were asked to assess the realism of oil and honey rendering without having experienced walking through them in real life. Even for water, the most recent real-world experience is likely too long ago to serve as a reference. Without a good reference of how the experience is supposed to feel, rating its realism becomes practically impossible. Not knowing which fluid environment is being rendered in the first place does not help with scoring its realism either.

Lastly, it appears that the model with counterflow was perceived as the least realistic. This likely reflects a mismatch between participant expectations and what was actually being rendered. As participants were not informed that the virtual fluid would flow toward them, they could not evaluate the realism accordingly. Notably, one participant mentioned during their first trial with counterflow that it ”suddenly felt like they had to move against a strong headwind,” which accurately describes how the counterflow is supposed to feel. This suggests that if participants had been informed what they were supposed to feel, they might have given higher realism scores.

5.3.2 Perceived forces

The ratings of perceived forces (table 19) are also strongly affected by individual differences between participants. While one participant rated all forces as 4 or lower, another reported multiple scores of 9. However, interpersonal variation is not the only source of bias in the data. Fatigue also appears to have a strong influence on the perceived forces. As participants become fatigued, they are more likely to experience identical forces as stronger than when they are well-rested. Fatigue is also a plausible cause for the within-participant inconsistencies in the force ratings of the control trials. For a future, larger-scale experiment, the force ratings should therefore be corrected for fatigue to enable a meaningful statistical analysis.

Another notable observation is that there were multiple instances of two or more fluid conditions from the same model receiving (nearly) identical force ratings. This could indicate that the simulated fluid environments are too similar to be distinguishable. To investigate this, it would be valuable to experimentally determine the Weber fraction (the minimum perceptible relative change) for differentiating virtual viscosities rendered with the exoskeleton, similar to the approach used by Schmidt *et al.* [38] for a hand–arm exoskeleton. Such an analysis could clarify whether the haptic rendering gain (i.e., the mapping between desired torque and angular displacement) should be retuned to enhance the perceptual distinction between fluid conditions.

5.3.3 Identification of fluid environments

Table 18 shows the guesses each participant made in identifying the fluid environment for each trial. With 9 out of 15 trials identified correctly, the model with counterflow has the most correct guesses of all the models. This is primarily the result of the counterflowing honey environment being so heavy to walk in that it is easily identified correctly. For all other models, the environments with honey or oil were never identified correctly. This is most likely because they are the fluids that the participants have never walked through in real-life, making it much harder to identify them through a haptic experience. The air environment was identified correctly about two-thirds of the time, independently of the rendering model. So participants are fairly consistent in their ability to identify the control trials as such, even if their subjective realism and force ratings are not.

The level of confidence does not appear to be a good predictor for how many of the guesses are correct, as the only set of guesses with a confidence level of 3 (very confident) had no correct guesses at all.

6 Conclusion

In this study, an Aquatic treadmill walking model was developed to enable the haptic rendering of fluid environments on a lower limb exoskeleton. The Aquatic treadmill walking model is a physics-based computational model that can simulate the forces of drag and/or buoyancy experienced while walking on a treadmill through a virtual fluid. A variety of fluid environments can be simulated using this model, varying in depth, flow velocity and the fluid’s density and viscosity. The model uses slightly different virtual leg kinematics compared to the conventional free walking kinematics found in the literature, making it more suitable for haptic applications where the user is walking on a treadmill. Through simulations, it was demonstrated that the model’s simulated output torques and forces are consistent with the literature and scale as expected when environment parameters are changed.

The aquatic treadmill walking model was successfully integrated into the existing control architecture of the exoskeleton, and a pilot experiment was run as a proof of concept. This experiment evaluated the haptic experience of three healthy participants walking in the exoskeleton while the aquatic treadmill model or a simpler proportional resistance model rendered a variety of fluid environments. However, a larger-scale experiment is required to draw any conclusions on whether either of the models is perceived as more realistic.

Compared to the existing literature, this implementation of haptically rendering fluid environments on a lower limb exoskeleton adds lateral degrees of freedom on top of the previously explored sagittal degrees of freedom. This enables simulating the balancing effects of aquatic therapy on the robot, and opens up a new area of exploration for virtual aquatic gait rehabilitation therapies.

References

[1] V. L. Feigin *et al.*, "World stroke organization (WSO): Global stroke fact sheet 2022," *International Journal of Stroke*, vol. 17, no. 1, pp. 18–29, Jan. 2022, ISSN: 1747-4930, 1747-4949.

[2] P. W. Duncan *et al.*, "Protocol for the locomotor experience applied post-stroke (LEAPS) trial: A randomized controlled trial," *BMC Neurology*, vol. 7, no. 1, p. 39, Dec. 2007, ISSN: 1471-2377.

[3] T. Zapata, N. A. Muscat, M. Falkenbach, and M. Wismar, "From great attrition to great attraction: Countering the great resignation of health and care workers," in Eurohealth, vol. 19, no. 1, pp. 6-10, 2023.

[4] L. Marchal-Crespo and R. Riener, "Technology of the robotic gait orthosis lokomat," in *Neurorehabilitation Technology*, D. J. Reinkensmeyer, L. Marchal-Crespo, and V. Dietz, Eds., Springer International Publishing, 2022, pp. 665–681, ISBN: 978-3-031-08994-7.

[5] M. A. Guadagnoli and T. D. Lee, "Challenge point: A framework for conceptualizing the effects of various practice conditions in motor learning," *Journal of Motor Behavior*, vol. 36, no. 2, pp. 212–224, Jul. 2004, ISSN: 1940-1027.

[6] B. E. Becker, "Aquatic therapy: Scientific foundations and clinical rehabilitation applications," *PM&R*, vol. 1, no. 9, pp. 859–872, Sep. 2009, ISSN: 1934-1482.

[7] M. I. V. Orselli and M. Duarte, "Joint forces and torques when walking in shallow water," *Journal of Biomechanics*, vol. 44, no. 6, pp. 1170–1175, Apr. 2011, ISSN: 0021-9290.

[8] C. S. Chae, J. H. Jun, S. Im, Y. Jang, and G.-Y. Park, "Effectiveness of hydrotherapy on balance and paretic knee strength in patients with stroke: A systematic review and meta-analysis of randomized controlled trials," *American Journal of Physical Medicine & Rehabilitation*, vol. 99, no. 5, pp. 409–419, May 2020, ISSN: 1537-7385.

[9] F. Salgado-Gomes-Sagaz, V. Zorrilla-Muñoz, and N. Garcia-Aracil, "Rehabilitation technologies by integrating exoskeletons, aquatic therapy, and quantum computing for enhanced patient outcomes," *Sensors*, vol. 24, no. 23, p. 7765, Dec. 4, 2024, ISSN: 1424-8220.

[10] K. Kong, H. Moon, D. Jeon, and M. Tomizuka, "Control of an exoskeleton for realization of aquatic therapy effects," *IEEE/ASME Transactions on Mechatronics*, vol. 15, no. 2, pp. 191–200, Apr. 2010, ISSN: 1083-4435.

[11] K. Kong, H. Moon, B. Hwang, D. Jeon, and M. Tomizuka, "Impedance compensation of SUBAR for back-drivable force-mode actuation," *IEEE Transactions on Robotics*, vol. 25, no. 3, pp. 512–521, Jun. 2009, ISSN: 1552-3098.

[12] M. Chang and D. Jeon, "The realization of virtual environments in the lower limb exoskeletal robot," 2025.

[13] T. E. Ertop, T. Yuksel, and E. I. Konukseven, "Realization of human gait in virtual fluid environment on a robotic gait trainer for therapeutic purposes," *Robotics and Autonomous Systems*, vol. 105, pp. 59–68, Jul. 2018, ISSN: 0921-8890.

[14] B. Luciani *et al.*, "Personalized gait patterns during exoskeleton-aided training may have minimal effect on user experience. insights from a pilot study," 2025.

[15] D. Wyss, "Enabling balance training in robot-assisted gait rehabilitation," ETH Zurich, Ph.D. dissertation, Mar. 2019.

[16] B. Siciliano, L. Sciavicco, L. Villani, and G. Oriolo, *Robotics: Modelling, Planning and Control* (Advanced Textbooks in Control and Signal Processing). Springer, 2010, ISBN: 978-1-84996-634-4.

[17] U. Patel, F. Sup, and Y. Modarres-Sadeghi, "Numerical simulation of flow around the legs during walking in water with implications for hydrotherapeutic exercise," Jan. 18, 2024.

[18] J. Stam, "Real-time fluid dynamics for games," in Proceedings of the game developer conference, vol. 18, no. 11, 2003.

[19] J. J. Monaghan, "Smoothed particle hydrodynamics," *Reports on Progress in Physics*, vol. 68, no. 8, pp. 1703–1759, Aug. 1, 2005, ISSN: 1361-6633.

[20] P. Xia, "New advances for haptic rendering: State of the art," *Visual Computer*, vol. 34, no. 2, pp. 271–287, Oct. 2018, ISSN: 1432-2315.

[21] D. Young, B. Munson, and T. Okiishi, *A Brief Introduction To Fluid Mechanics, 5th Edition*. John Wiley & Sons, 2010, ISBN: 978-1-118-14010-9.

[22] K. O. L. F. Jayaweera and B. J. Mason, "The behaviour of freely falling cylinders and cones in a viscous fluid," *Journal of Fluid Mechanics*, vol. 22, no. 4, pp. 709–720, Aug. 1965, ISSN: 1469-7645.

[23] D. J. Tritton, "Experiments on the flow past a circular cylinder at low reynolds numbers," *Journal of Fluid Mechanics*, vol. 6, no. 4, pp. 547–567, Nov. 1959, ISSN: 1469-7645.

[24] C. Wieselsberger, "New data on the laws of fluid resistance," Aerodynamic Institue, Gottingen, NACA-TN-84, Mar. 1922.

[25] K. Akiyama, M. Nakashima, and T. Miyoshi, "Simulation analysis of the mechanical body load during walking in water," *Journal of Environment and Engineering*, vol. 6, no. 2, pp. 365–375, 2011, ISSN: 1880-988X.

[26] J. Lauer, "Video-driven simulation of lower limb mechanical loading during aquatic exercises," *Journal of Biomechanics*, vol. 152, p. 111 576, May 2023, ISSN: 00219290.

[27] M. Nakashima, K. Satou, and Y. Miura, "Development of swimming human simulation model considering rigid body dynamics and unsteady fluid force for whole body," *Journal of Fluid Science and Technology*, vol. 2, no. 1, pp. 56–67, 2007, ISSN: 1880-5558.

[28] S. Woernle, "Subjective assessment of individualized gait patterns on enjoyment, comfort, and naturalness in robot-assisted walking," TU Delft, MSc thesis, Mar. 2023.

[29] C. A. Fukuchi, R. K. Fukuchi, and M. Duarte, "A public dataset of overground and treadmill walking kinematics and kinetics in healthy individuals," *PeerJ*, vol. 6, Apr. 24, 2018, ISSN: 2167-8359.

[30] S. Fantozzi, A. Giovanardi, D. Borra, and G. Gatta, "Gait kinematic analysis in water using wearable inertial magnetic sensors," *PLOS ONE*, vol. 10, no. 9, D. Heymann, Ed., e0138105, Sep. 14, 2015, ISSN: 1932-6203.

[31] T. Jung, Y. Kim, H. Lim, and K. Vrongistinos, "The influence of water depth on kinematic and spatiotemporal gait parameters during aquatic treadmill walking," *Sports Biomechanics*, vol. 18, no. 3, pp. 297–307, May 4, 2019, ISSN: 1476-3141, 1752-6116.

[32] B. C. L. So *et al.*, "A study comparing gait and lower limb muscle activity during aquatic treadmill running with different water depth and land treadmill running," *Journal of Human Kinetics*, vol. 82, pp. 39–50, Apr. 2022, ISSN: 1640-5544.

[33] "PlotDigitizer: Version 3.1.5," 2025.

[34] MathWorks Inc., "MATLAB and Simulink Release R2013b," 2013.

[35] T. Shi and O. Schneider, "Development and initial validation of the haptic experience inventory (HXI)," in *Proceedings of the 2025 CHI Conference on Human Factors in Computing Systems*, Yokohama Japan: ACM, Apr. 26, 2025, pp. 1–21, ISBN: 979-8-4007-1394-1.

[36] G. A. V. Borg, *Borg's Perceived exertion and pain scales*. Champaign, Ill.: Human Kinetics, 1998, 104 pp., ISBN: 978-0-88011-623-7.

[37] R. J. Marley and N. Kumar, "An improved musculoskeletal discomfort assessment tool," *International Journal of Industrial Ergonomics*, vol. 17, no. 1, pp. 21–27, Jan. 1996, ISSN: 01698141.

[38] A. Schmidt *et al.*, "Enabling interaction with virtual fluids and mixed media using a high dexterity hand exoskeleton," in *Conference Proceedings - IEEE International Conference on Systems, Man and Cybernetics*, vol. 2020-October, 2020, pp. 2925–2932, ISBN: 978-1-72818-526-2.

Appendix A: Virtual Leg Kinematics

The inertial origin of the kinematic model is located at the centre of the pelvis when the user stands upright in the anatomical reference pose. The virtual pelvis frame of reference is also centred in the middle of the pelvis between the two hip joints, but moves along with the physical pelvis of the user, and is visualised in fig. 8.

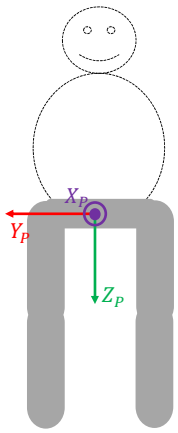

Figure 8: Visualisation of the position and orientation of the virtual pelvis frame (as seen from the front)

The virtual pelvis is defined as a rigid body that can freely move with respect to the inertial origin of the virtual environment. This means that its position and orientation are described by a set of 6 degrees of freedom: The x, y, and z position of the pelvis midpoint (x_p, y_p, and z_p), and the rotation around the inertial x, y, and z axes compared to the anatomical reference pose (φ_p, θ_p, and ψ_p). Since the pelvis does not move forward in the walking on a treadmill model, the x-displacement should remain 0. However, to allow for some play, it is still included in the kinematic model. The same is true for the rotations. They should also be roughly 0, but are included for completeness. The homogeneous transformation (${}^{O}T_{P1}$) from the inertial origin frame (O) to the pelvis frame (P) is given by the matrix multiplication in eq. (12). This is done using three in-between frames: $P1$, $P2$, and $P3$, each of which represents one of the three consecutive rotations. The consecutive homogeneous transformations are defined by the matrices in eq. (13). Note that the order in which the rotations are applied is Z-X-Y (Yaw-Pitch-Roll).

$$ {}^{O}T_{P} = {}^{O}T_{P1} \cdot {}^{P1}T_{P2} \cdot {}^{P2}T_{P3} \tag{12} $$

$$ {}^{O}T_{P1} = \begin{bmatrix} \cos(\psi_p) & \sin(\psi_p) & 0 & x_p \\ -\sin(\psi_p) & \cos(\psi_p) & 0 & y_p \\ 0 & 0 & 1 & z_p \\ 0 & 0 & 0 & 1 \end{bmatrix} \tag{13a} $$

$$ {}^{P1}T_{P2} = \begin{bmatrix} \cos(\theta_p) & 0 & \sin(\theta_p) & 0 \\ 0 & 1 & 0 & 0 \\ -\sin(\theta_p) & 0 & \cos(\theta_p) & 0 \\ 0 & 0 & 0 & 1 \end{bmatrix} \tag{13b} $$

$$ {}^{P2}T_{P3} = \begin{bmatrix} 1 & 0 & 0 & 0 \\ 0 & \cos(\varphi_p) & \sin(\varphi_p) & 0 \\ 0 & -\sin(\varphi_p) & \cos(\varphi_p) & 0 \\ 0 & 0 & 0 & 1 \end{bmatrix} \tag{13c} $$

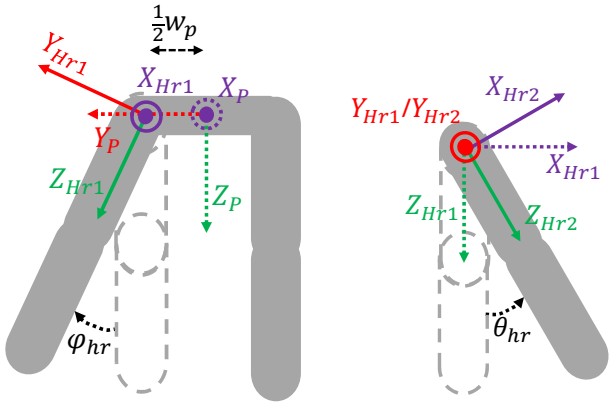

a) Position and orientation of the $Hr1$ frame (as seen from the front)

b) Orientation of the $Hr2$ frame (as seen from the right)

Figure 9: Illustration of the position and orientation of the two right hip frames. The position and orientation of the left hip frames are equivalent, but with a translation in the negative y direction and an abduction angle around the positive x-axis.

At either end of the pelvis, there is a hip joint with two degrees of freedom: abduction and flexion. For both hips, the flexion angle (θ_{hl} and θ_{hr} for the left and right hip, respectively) goes around the positive y-axis, and the abduction angle goes around the positive x-axis for the left hip (φ_{hl}) and the negative x-axis for the right hip (φ_{hr}). The hip joints are situated at half a pelvis width (w_p) distance from the pelvis midpoint in the positive and negative y-direction. There are two frames of reference associated with each hip, as illustrated in fig. 9 for the right hip. Frame $Hr1$ moves with the abduction of the (right) hip compared to the pelvis frame (P). Frame $Hr2$ moves with the flexion of the (right) hip compared to $Hr1$.

The transformation matrices to go from frame P to $Hr1$ and from $Hr1$ to $Hr2$ are given in eq. (15) and eq. (16), respectively. The transformation matrix from the inertial frame (O) to the right hip frame (Hr) is then given by eq. (14).

$$ {}^{O}T_{Hr} = {}^{O}T_{P} \cdot {}^{P}T_{Hr1} \cdot {}^{Hr1}T_{Hr2} \tag{14} $$

$$ {}^{P}T_{Hr1} = \begin{bmatrix} 1 & 0 & 0 & 0 \\ 0 & \cos(\varphi_{hr}) & \sin(\varphi_{hr}) & \frac{1}{2}w_p \\ 0 & -\sin(\varphi_{hr}) & \cos(\varphi_{hr}) & 0 \\ 0 & 0 & 0 & 1 \end{bmatrix} \tag{15} $$

$$ {}^{Hr1}T_{Hr2} = \begin{bmatrix} \cos(\theta_{hr}) & 0 & \sin(\theta_{hr}) & 0 \\ 0 & 1 & 0 & 0 \\ -\sin(\theta_{hr}) & 0 & \cos(\theta_{hr}) & 0 \\ 0 & 0 & 0 & 1 \end{bmatrix} \tag{16} $$

The transformation matrices for the left hip frame(s) are very similar, except that the translation in the y-direction is reversed, and the abduction goes around the positive x-axis instead of the negative one. The matrices are thus given by eqs. (17) to (19).

$$ {}^{O}T_{Hl} = {}^{O}T_{P} \cdot {}^{P}T_{Hl1} \cdot {}^{Hl1}T_{Hl2} \tag{17} $$

$$ {}^{P}T_{Hl1} = \begin{bmatrix} 1 & 0 & 0 & 0 \\ 0 & \cos(\varphi_{hl}) & -\sin(\varphi_{hl}) & -\frac{1}{2}w_p \\ 0 & \sin(\varphi_{hl}) & \cos(\varphi_{hl}) & 0 \\ 0 & 0 & 0 & 1 \end{bmatrix} \tag{18} $$

$$ {}^{Hl1}T_{Hl2} = \begin{bmatrix} \cos(\theta_{hl}) & 0 & \sin(\theta_{hl}) & 0 \\ 0 & 1 & 0 & 0 \\ -\sin(\theta_{hl}) & 0 & \cos(\theta_{hl}) & 0 \\ 0 & 0 & 0 & 1 \end{bmatrix} \tag{19} $$

The last frames to consider are the knee frames, which are positioned at 1 thigh length (L_t) in z-direction in the hip frame of the same leg. Their orientation moves along with the flexion of the respective knee (θ_{kl} and θ_{kr} for left and right). This position and orientation are illustrated in fig. 10.

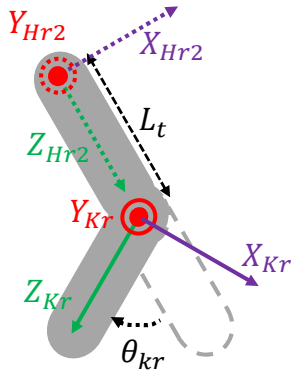

Figure 10: Illustration of the position and orientation of the right knee frame (Kr) compared to the second right hip frame ($Hr2$), as seen from the right. The position and orientation of the left knee frame are defined in the same way.

The transformation matrix from the right hip frame Hr to the right knee frame is given by eq. (21). The transformation matrix to go from the inertial frame O to the right knee frame can then be computed through eq. (20).

$$ {}^{O}T_{Kr} = {}^{O}T_{Hr} \cdot {}^{Hr}T_{Kr} \tag{20} $$

$$ {}^{Hr}T_{Kr} = \begin{bmatrix} \cos(\theta_{kr}) & 0 & -\sin(\theta_{kr}) & 0 \\ 0 & 1 & 0 & 0 \\ \sin(\theta_{kr}) & 0 & \cos(\theta_{kr}) & L_t \\ 0 & 0 & 0 & 1 \end{bmatrix} \tag{21} $$

Likewise, eq. (23) gives the transformation matrices from the left hip frame Hl to the left knee frame Kl, and eq. (22) can be used to compute the transformation from the inertial frame O to the left knee frame.

$$ {}^{O}T_{Kl} = {}^{O}T_{Hl} \cdot {}^{Hl}T_{Kl} \tag{22} $$

$$ {}^{Hl}T_{Kl} = \begin{bmatrix} \cos(\theta_{kl}) & 0 & -\sin(\theta_{kl}) & 0 \\ 0 & 1 & 0 & 0 \\ \sin(\theta_{kl}) & 0 & \cos(\theta_{kl}) & L_t \\ 0 & 0 & 0 & 1 \end{bmatrix} \tag{23} $$

Appendix B: Gait Cycle Time Estimation

For every trial of every participant in the gait database from Fukuchi *et al.* [29], the walking speed and gait cycle time are shown as a scatterplot in fig. 11. A power law function was fitted through these data points to describe the relation between walking speed and gait cycle time. This relation was then used to extrapolate the expected gait cycle time for walking at a speed of 0.31 $\mathrm{m\,s^{-1}}$.

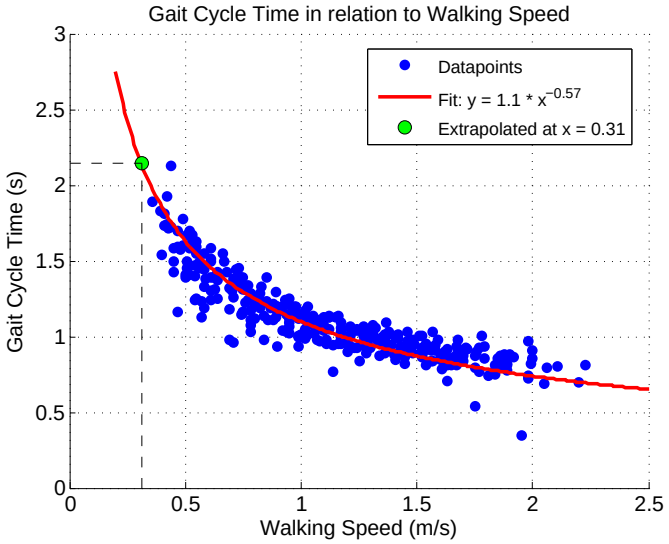

Figure 11: A scatterplot of the gait cycle time and walking speed for all trials included in the gait database from Fukuchi *et al.* [29]. Each blue dot is one trial from that database. The red line is a power series fit through this data, which is used to extrapolate the gait cycle time for a walking speed of 0.31 $\mathrm{m\,s^{-1}}$, shown in green.

Appendix C: Simulation Input Kinematics

The simulation in phase 1 is run using the kinematic data from Akiyama *et al.* [25]. After data extraction, subsampling, and smoothing, the resulting gait cycle kinematics used as input for the simulation are shown in fig. 12. As no data for the hip abduction and pelvis displacement are reported, they are both assumed to be a constant 0 in the simulation.

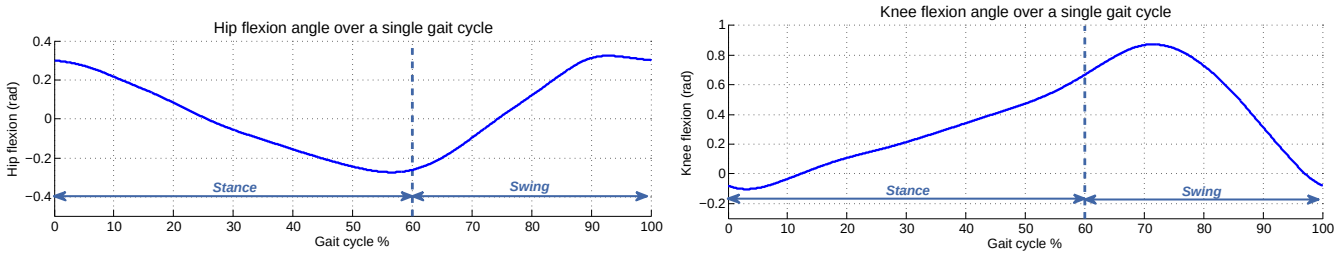

a) Hip flexion angle

b) Knee flexion angle

Figure 12: The kinematic data extracted from Akiyama *et al.* [25], which is used as a kinematic input in simulation phase 1. The gait cycle goes from heel strike to heel strike, with toe-off occurring at 60%.

The simulations in phases 2 and 3 are run using kinematic data from Woernle [28]. After data extraction, subsampling, and smoothing, the resulting gait cycle kinematics used as input for the simulation are shown in fig. 13.

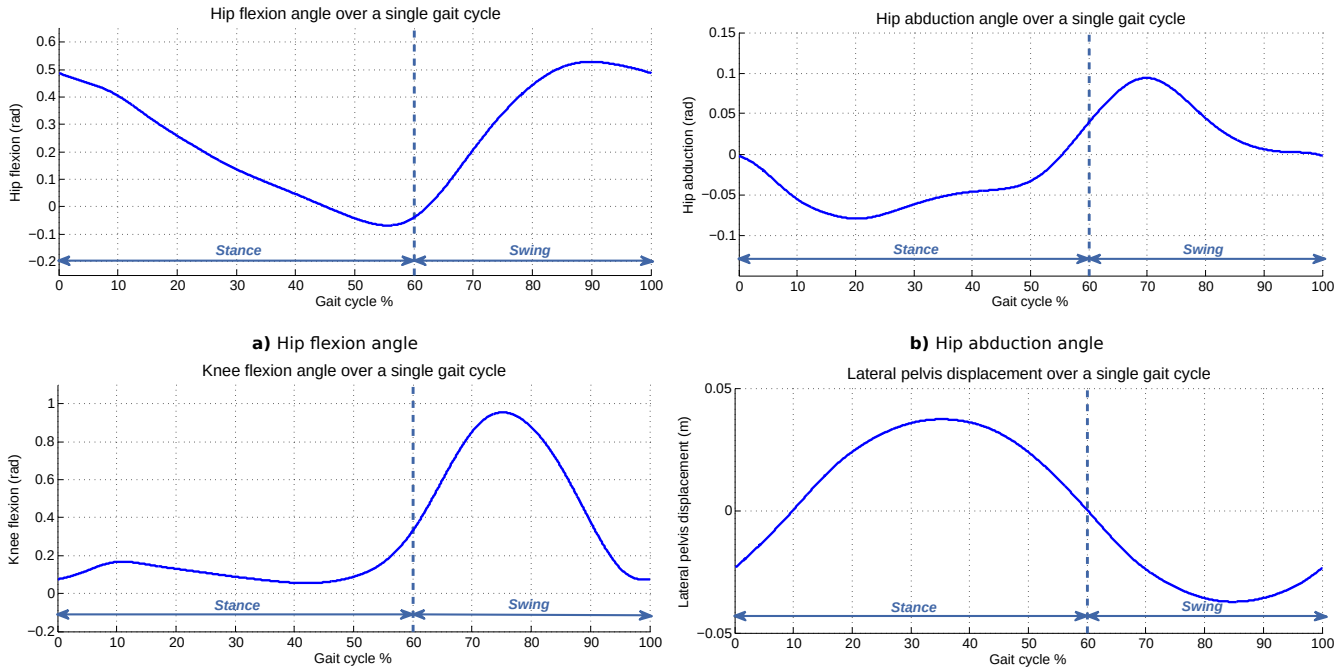

a) Hip flexion angle

b) Hip abduction angle

c) Knee flexion angle

d) Lateral pelvis displacement

Figure 13: The kinematic data extracted from Woernle [28], which is used as a kinematic input in simulation phases 2 and 3. The gait cycle goes from heel strike to heel strike, with toe-off occurring at 60%.

Appendix D: Simulation Results - Graphs

These are the graphs of the fluid torque contributions of drag and buoyancy to each joint computed by the model during the various simulations in phases 2 and 3 of the model validation.

Baseline Simulation

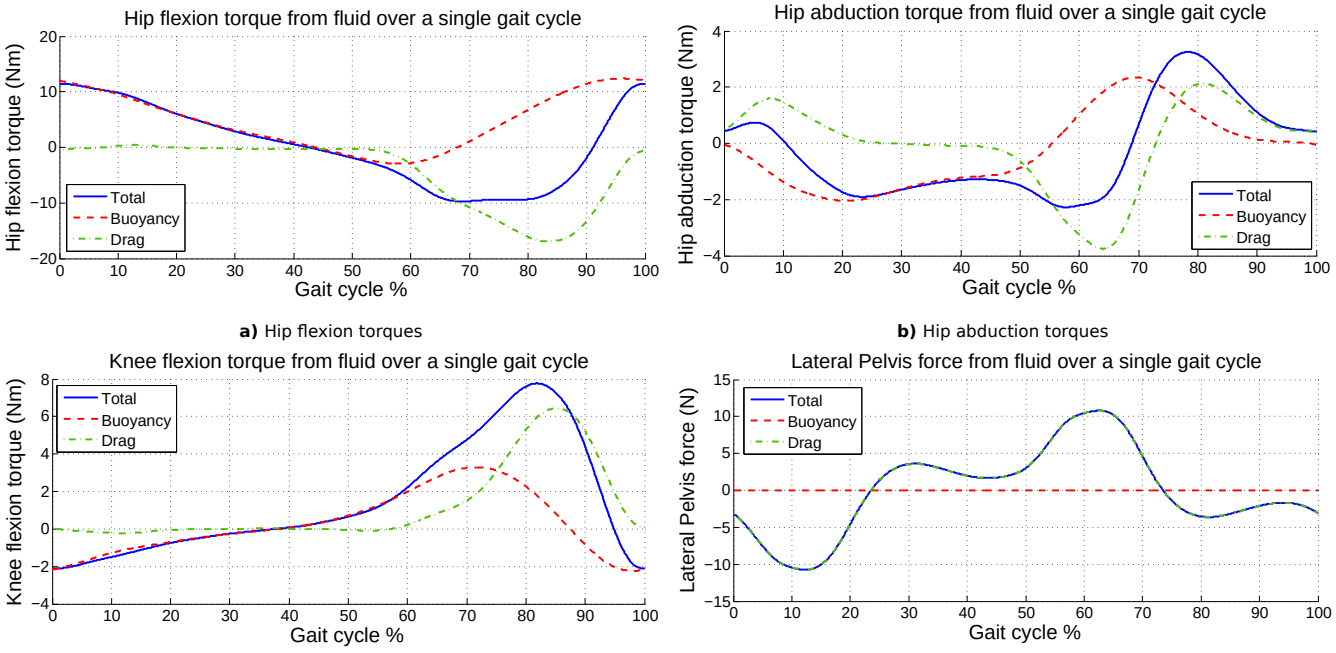

a) Hip flexion torques

b) Hip abduction torques

c) Knee flexion torques

d) Lateral pelvis forces

Figure 14: The baseline simulation results for waist-deep water using the kinematics from Woernle [28]. For each joint, both the total torque and the individual contributions of drag and buoyancy are shown.

Double movement speed

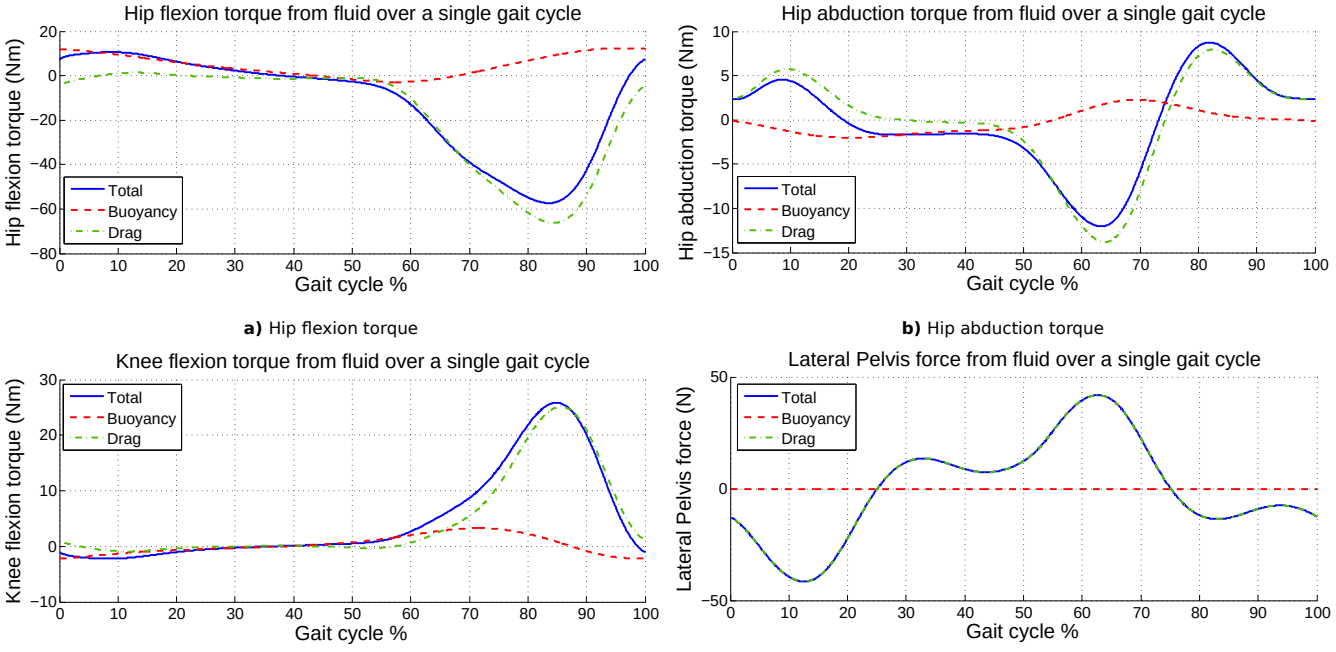

a) Hip flexion torque

b) Hip abduction torque

c) Knee flexion torque

d) Lateral pelvis force

Figure 15: The simulation results for walking at double the speed (0.62 $\mathrm{m\,s^{-1}}$). For each joint, both the total torque and the individual contributions of drag and buoyancy are shown.

Knee-deep Water

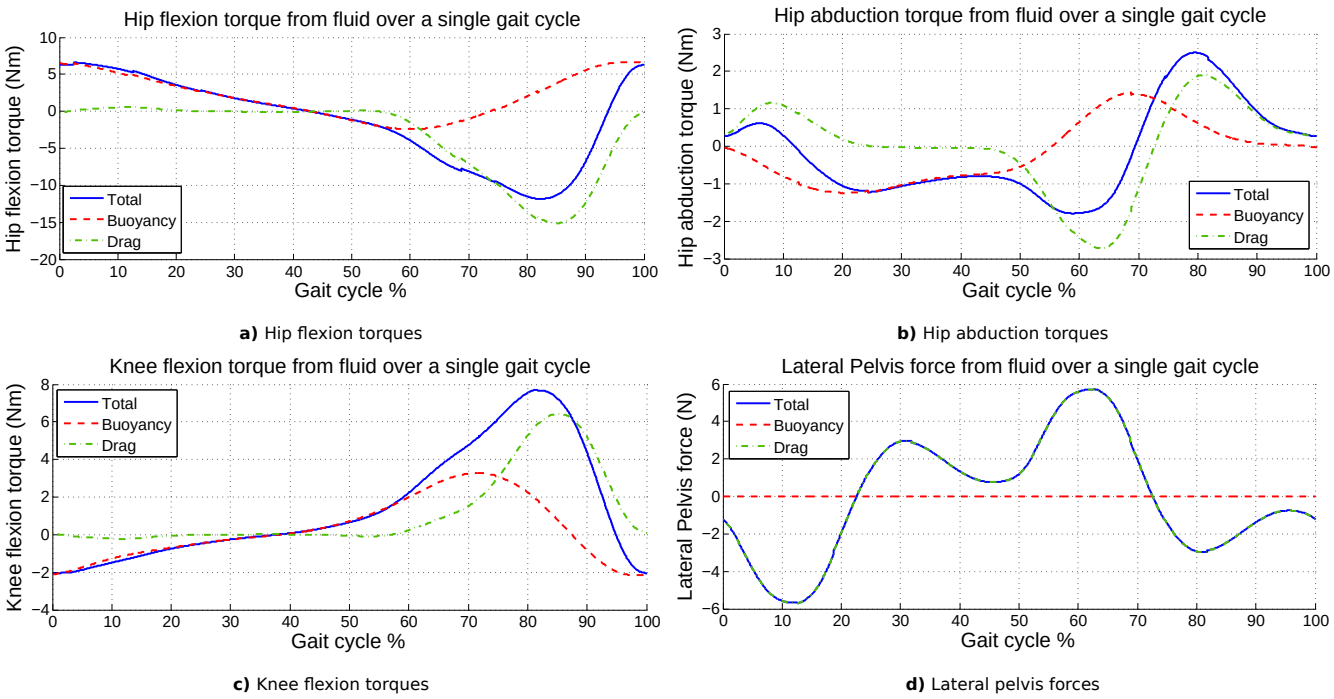

a) Hip flexion torques

b) Hip abduction torques

c) Knee flexion torques

d) Lateral pelvis forces

Figure 16: The simulation results for walking in knee-deep water. For each joint, both the total torque and the individual contributions of drag and buoyancy are shown.

Waist-deep Olive Oil

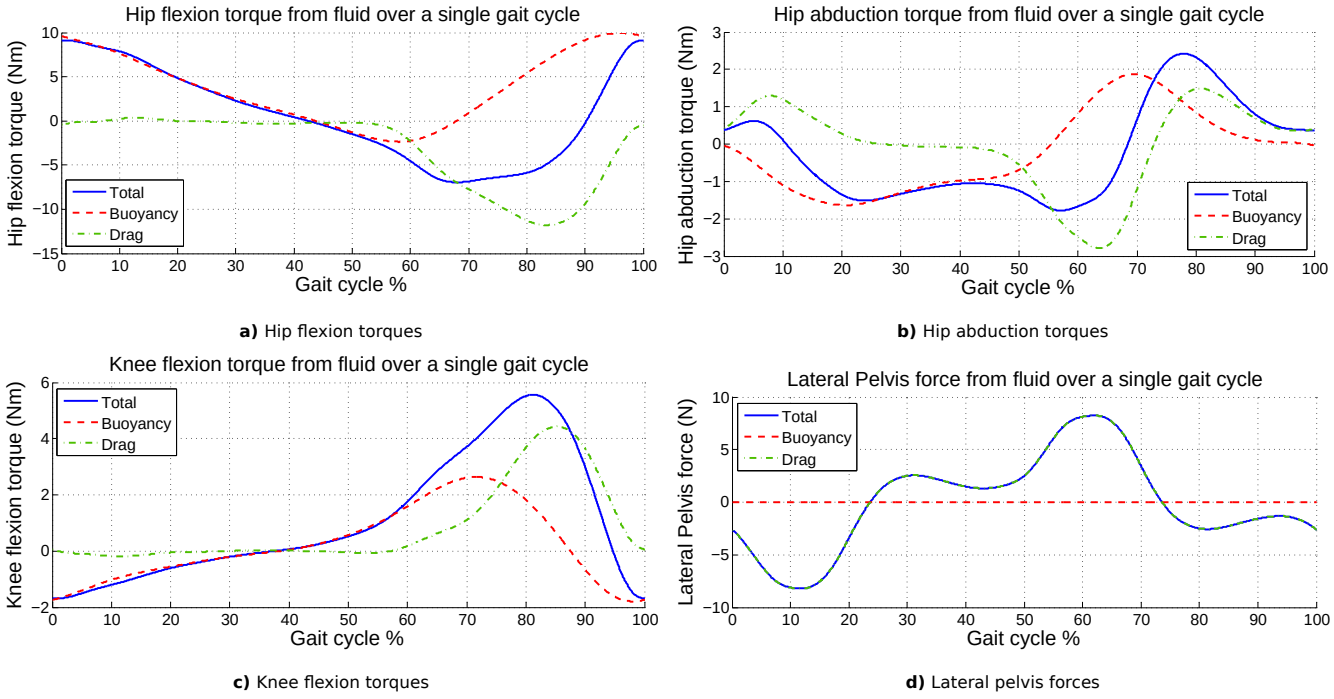

a) Hip flexion torques

b) Hip abduction torques

c) Knee flexion torques

d) Lateral pelvis forces

Figure 17: The simulation results for waist-deep olive oil. For each joint, both the total torque and the individual contributions of drag and buoyancy are shown.

Waist-deep Honey

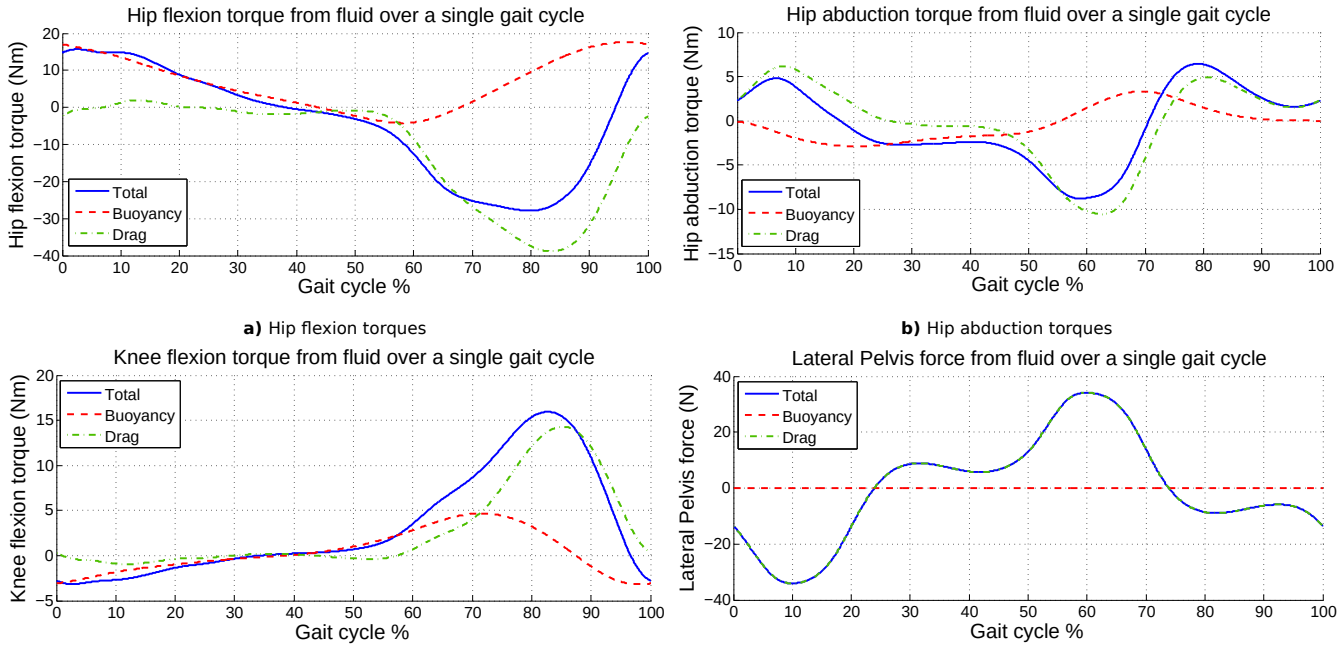

a) Hip flexion torques

b) Hip abduction torques

c) Knee flexion torques

d) Lateral pelvis forces

Figure 18: The simulation results for waist-deep honey. For each joint, both the total torque and the individual contributions of drag and buoyancy are shown.

Waist-deep Peanut Butter

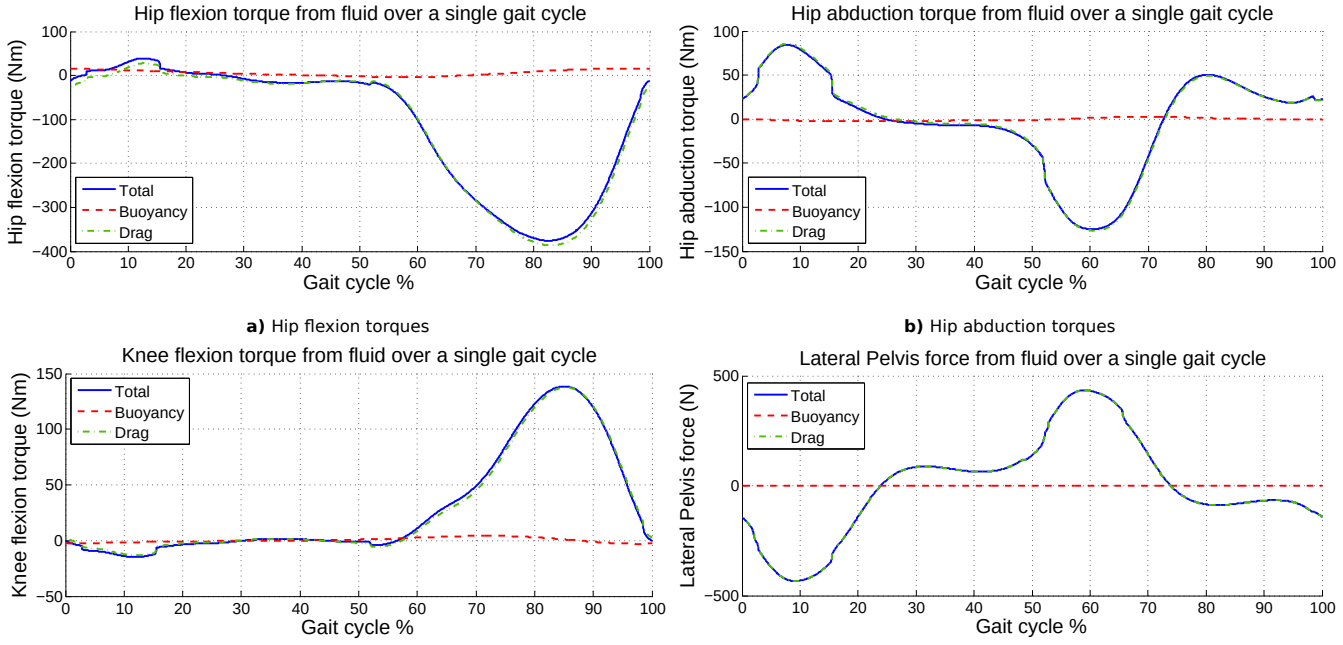

a) Hip flexion torques

b) Hip abduction torques

c) Knee flexion torques

d) Lateral pelvis forces

Figure 19: The simulation results for waist-deep peanut butter. For each joint, both the total torque and the individual contributions of drag and buoyancy are shown.

Appendix E: Proportional Resistance Model

During the pilot experiment, the quality of the haptic rendering of the model developed in this research and its perceived resistance are compared to those of a simpler proportional resistance model. This appendix describes the proportional resistance model in more detail.

The proportional resistance model is intended to be the easiest implementation of a model that can haptically render a fluid resistance. It fully disregards buoyancy and instead only renders drag. Also, many simplifications are made in the drag. Firstly, it is assumed that the behaviour of the knee joint does not influence the drag experienced at the hip and vice versa. In reality, the hip and knee joints both influence the velocity of the shank, and thus the drag forces applied there. The drag forces at the shank also result in a torque experienced at both the knee and hip joints. So in reality, the hip and knee joints both have a big influence on the torques experienced by the other. In the simple proportional model, on the other hand, the torque at the hip (τ_{hip}) is quadratically proportional to the hip joint's angular velocity (ω_{hip}) via a gain $k_{d,hip}$ and a fluid-dependent multiplier x, and similarly for the knees. Likewise, the drag force at the pelvis (F_{pelvis} is quadratically proportional to the linear velocity of the pelvis (u_{pelvis}), as denoted by eq. (24). The value of the multiplier is determined by the simulation results of Chang and Jeon [12]. For water, the multiplier x is 1, and for the other fluids it is equal to the drag multiplier listed in table 5.

$$\begin{aligned} \tau_{hipflex} &= x\, k_{d,hip\,flex}\, \omega_{hip\,flex}\, ||\omega_{hip\,flex}|| \\ \tau_{hipabd} &= x\, k_{d,hip\,abd}\, \omega_{hip\,abd}\, ||\omega_{hip\,abd}|| \\ \tau_{knee} &= x\, k_{d,knee}\, \omega_{knee}\, ||\omega_{knee}|| \\ F_{pelvis} &= x\, k_{d,pelvis}\, u_{pelvis}\, ||u_{pelvis}|| \end{aligned} \tag{24}$$

The gains were tuned through simulation, such that the peak torques were in the same order of magnitude as those from the aquatic walking model given the kinematic inputs from Woernle [28]. The values of those gains are listed in

Table 11: Proportional gains k_d of the simple model

Gain	Value
$k_{d,hipflex}$	-5
$k_{d,hipabd}$	-13
$k_{d,knee}$	-1
$k_{d,pelvis}$	-600

Simulating the simple model with these gains for waist-deep water, using the kinematics from Woernle [28], yields the output forces and torques shown in fig. 20. Most notably, due to the simplifications described above, the buoyancy component is 0 for all degrees of freedom, and the shapes of the drag component curves are very different from those in fig. 14 that were simulated using the aquatic walking model. Looking at the relative peak torque differences, the values in table 12 are obtained.

Table 12: The peak value of each torque component and the total torque in the waist-deep water simulation using the simple model relative to the peak value of the same torque component in the same simulation using the aquatic walking model. The values given are those of the multiplier x in eq. (11).

	Drag	Buoyancy	total
Hip flexion torque	0.54	0	0.80
Hip abduction torque	0.58	0	0.67
Knee flexion torque	1.20	0	1.00
Lateral pelvis force	0.88	-	0.88

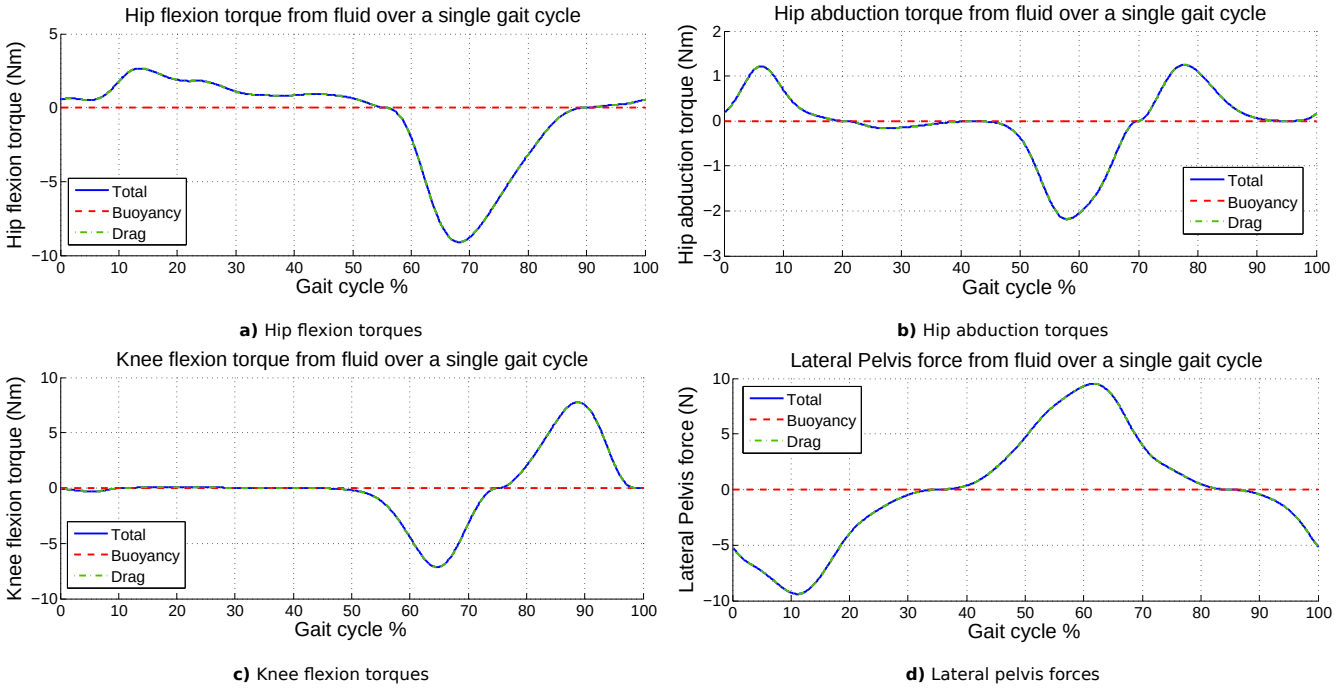

a) Hip flexion torques

b) Hip abduction torques

c) Knee flexion torques

d) Lateral pelvis forces

Figure 20: The simulation results for waist-deep water, using the simple proportional resistance model. Note that buoyancy is not considered in this model, hence why it is zero for all degrees of freedom.

After testing on the exoskeleton itself, it was determined that with these gains, the knee flexion was too stiff, making it uncomfortably hard to bend the knees, especially with more viscous fluids being rendered. Therefore, the knee gain was reduced to -0.4.

Appendix F: Exoskeleton Start-up Procedure

Table 13 lists the steps required to start the exoskeleton such that it can be used for virtual fluid rendering.

Table 13: Exoskeleton Start-up checklist for turning on virtual aquatic therapy rendering

#	Task	Done
1	Turn on the host PC, log in, and open MATLAB R2013b	☐
2	Turn on the exoskeleton via the power block	☐
3	Make sure both emergency stops are not pressed	☐
4	Turn on the exoskeleton target xPC	☐
5	Check that the target PC booted correctly. If it got stuck mid-boot, turn it off and on again, until it does boot properly	☐
6	In MATLAB, run init_ForceControl.m	☐
7	Check that you now see 4 GUI windows: The LokoFree Control GUI, the fluid rendering GUI, the Disturbance Control GUI, and the Treadmill Control GUI	☐
8	In the LokoFree Control GUI, make sure the selected model is LokoFree_ForceControl_aquatic_with_simple	☐
9	If changes were made to the model, navigate to the build folder, open the Simulink model and rebuild it. Otherwise, you can skip this step.	☐
10	In the LokoFree Control GUI, click load exoskeleton to download the Simulink model onto the xPC	☐
11	Check that the xPC monitor now shows a GUI with 9 value monitoring blocks. If not, load again	☐
12	In the LokoFree Control GUI, click start exoskeleton	☐
13	Check that the value monitoring blocks on the xPC monitor are now showing values	☐
14	In the Fluid rendering GUI, make sure both logging and fluid rendering are disabled	☐
15	Fill in the number of ticks for each exoskeleton segment into the LokoFree control GUI, put a checkmark in the MUCDA sensors and ATI mounted R checkbox (and not the ATI mounted L checkbox), and click set values to xPC	☐
16	In the Treadmill control GUI, click load treadmill	☐
17	Check that the treadmill monitor now shows a GUI with 4 value monitoring blocks. If not, load again	☐
18	In the Treadmill control GUI, click start treadmill	☐
19	Check that the value monitoring blocks on the treadmill monitor are now showing values	☐
20	In the LokoFree Control GUI, toggle the enableUnityUDP to off	
21	In the LokoFree Control GUI, clear the exoskeleton errors until no errors remain	☐

Appendix G: Experiment Protocol

The protocol for the experiment is listed in table 16. The protocol is divided into 6 phases. The steps in the preparations phase (A) and the system test phase (B) are done before the arrival of the participant. Once the participant is present, the steps in the pre-experiment phase (C) are followed. The steps in the trial phase (D) and between trials phase (E) are repeated for each trial in the experiment. Lastly, the post-experiment phase (F) is followed at the end, once the experiment is finished.

The experiment consists of 4 blocks of 5 trials each (for a total of 20 trials). Each block uses one of the four available rendering models, as listed in table 14. The order in which the models are used is randomised.

Table 14: The three rendering models used in the experiment

	Rendering model
A	Proportional resistance model
B	Aquatic Treadmill Walking model, without buoyancy or counterflow
C	Aquatic Treadmill Walking model, with buoyancy, but without counterflow
D	Aquatic Treadmill Walking model, with buoyancy, and with counterflow

Each trial within a block has a specific fluid condition that is rendered. The 5 fluid conditions are listed in table 15, and again appear in a random order for each block. Before the very first trial, there will be one familiarisation trial without fluid rendering enabled, so the participant can get used to walking with the exoskeleton (in transparency mode).

Table 15: The 5 fluid conditions that will be rendered in a random order for each block of the experiment

	Submersion level	**Rendered fluid**
1	No submersion	Air
2	Knee-deep	Water
3	Waist-deep	Water
4	Waist-deep	Honey
5	Waist-deep	Oil

The participant is given the following explanation of the experiment in step 4 of the pre-experiment phase:
"The experiment will consist of 20 trials in total, divided into 4 blocks of 5 trials each. During each trial, you will walk on the treadmill at a speed of 1 km/h for 60 seconds while strapped into the exoskeleton. The exoskeleton will apply forces to your legs and pelvis to create the feeling of being submerged in a virtual liquid. For each block of trials, a different rendering model is used, and for each trial within that block, a different fluid environment is rendered. Both the type of liquid and the depth of submersion will vary. The three liquids that will be rendered are water, oil, and honey. Oil is lighter than water, while honey is heavier and much more viscous. The depth of submersion will be either waist-deep, knee-deep, or nothing at all. After each trial, you will answer a few questions regarding perceived forces and perceived realism. After every block of 5 trials, there will be a short break, the duration of which will be up to you. During this break, I will ask you to identify which fluid you think was being rendered during each trial of the last block. At all times during the trials, both you and I will be holding an emergency stop button. If at any point, something feels unsafe, uncomfortable, or otherwise wrong, do not hesitate to press it. This will immediately stop the treadmill and the exoskeleton. Before we can start, I have a few demographic questions I would like you to answer. After that, I will invite you to stand on the treadmill so I can adjust the exoskeleton to you."

Table 16: Experiment protocol checklist

#	**Task**	**Done**
A	*Preparations*	
1	Print out this experiment protocol, the exoskeleton start-up procedure, and the questionnaire	☐
2	Bring at least two functioning pens for filling in the printed documents (one spare)	☐
3	Have a stopwatch and a tape measure ready	☐
4	Check that the body-weight support system, the harness, the orthosis, and the treadmill show no signs of damage	☐
5	Make sure the orange tension straps are loosely in place and show no signs of damage	☐
6	Make sure the data-logging USB drive is plugged into the target PC	☐
7	Randomise the order in which the models will appear and for each block of trials, in which order the fluid conditions will appear	☐

#	Task	Done
B	*System test*	
1	Follow the exoskeleton start-up procedure	☐
2	Check that the exoskeleton can freely be moved and that the transparency mode is working	☐
3	In the fluid rendering GUI, set the fluid environment to waist-deep water, using the Aquatic Treadmill walking model, with no buoyancy or counterflow, and enable fluid rendering	☐
4	Move the right leg of the exoskeleton and check that you can feel resistance due to the fluid rendering	☐
5	In the LokoFree control GUI, set the treadmill speed to 1 $\mathrm{km\,h^{-1}}$ and check that the treadmill starts moving	☐
6	Press the handheld emergency stop and check that the exoskeleton and treadmill stop moving	☐
7	Release the handheld emergency stop	☐
8	Clear exoskeleton errors via the LokoFree control GUI and check that the exoskeleton and treadmill become active again	☐
9	Press the floor emergency stop and check that the exoskeleton and treadmill stop moving	☐
10	Release the floor emergency stop and turn off the exoskeleton via the power block switch	☐
C	*Pre-experiment*	
1	Welcome the participant to the lab and thank them for making time to participate in the experiment	☐
2	Inform the participant that if at any point during the experiment they don't want to continue any more, they are free to quit	☐
3	Explain the setup of the experiment (important things to show: treadmill, exoskeleton (including how the participant will be strapped in), and emergency stops)	☐
4	Explain how the experiment will work (see text on the front page of this protocol)	☐
5	Check with the participant that they understand the experiment and still want to participate in it	☐
6	Ask the participant to fill in the Participant Demographic section of the questionnaire	☐
7	Ask the participant if there is anything (eg. medical condition) that the person running the experiment should know about before starting the experiment	☐
8	Let the participant know that if they want to can use a provided pair of sports shoes	☐
9	Ask the participant to stand on the treadmill between the legs of the exoskeleton, facing forward	☐
10	Adjust the height of the body weight support harness until it is at chest height	☐
11	Adjust the height of the pelvis with the tension straps, such that the hip joint of the exoskeleton is at the same height as the hip joint of the participant. Make sure to tighten them equally on both sides!	☐
12	Adjust the height of the pelvis module such that it is level with the pelvis	☐
13	Ask the participant to put on the body weight support harness (show them how to do this)	☐
14	Adjust the pelvis width of the exoskeleton such that it is a snug fit with the pelvis of the participant. Make sure that the number of ticks is the same on both sides!	☐
15	Adjust the frontal ticks of the pelvis such that the back of the participant rests against the pelvis backplate of the exoskeleton. Make sure that the number of ticks is the same on both sides!	☐
16	Adjust the length of the exoskeleton thighs such that the knee joints of the exoskeleton are at the same height as the knee joints of the participant	☐
17	Adjust the length of the exoskeleton shank such that the ankle cuff is just above the ankle of the participant	☐
18	Loosen the frontal sliders of the thigh, calf, and ankle cuffs	☐
19	Strap in the thigh, calf, and ankle cuffs, and ask the participant to straighten their legs	☐
20	Adjust the frontal ticks of the thigh cuffs such that the knee of the participant is right next to the knee joint of the exoskeleton, then tighten it	☐
21	Adjust the frontal ticks of the calf and ankle cuffs and tighten them again	☐
22	Ask the participant to make a walking motion with both their legs	☐
23	Ask if anything feels uncomfortable, and if so, adjust the exoskeleton accordingly	☐
24	Write down the number of ticks for each exoskeleton segment for future reference	☐
25	Start with a single familiarisation trial in transparency mode before starting with the trials with fluid rendering	☐

#	Task	Done
D	*Trials*	
1	If it is the first trial of a block, or if some error occurred during the previous trial (including pressing the emergency stops), follow steps 2 through 9 of the exoskeleton start-up procedure. Otherwise, you can skip those steps	☐
2	Hand the participant the hand-held emergency stop and remind them that if at any point in time they feel uncomfortable or unsafe, they should not hesitate to press it	☐
3	Grab the floor emergency stop yourself and make sure you are always able to press it if needed	☐
4	Follow steps 10 through 20 of the exoskeleton start-up procedure	☐
5	Fill in the trial ID in the logging section of the LokoFree control GUI (the trial ID is a 3-digit number, with the first digit the participant number, the second which block it is, and the third which trial it is within that block)	☐
6	In the fluid rendering GUI, enable logging	☐
7	In the fluid rendering GUI, adjust the fluid type, fluid depth, model selection, buoyancy enable, and counter-flow enable to the correct conditions for this trial and click the set values button	☐
8	Tell the participant that you will now enable the exoskeleton in transparency mode	☐
9	Clear the exoskeleton errors through the LokoFree control GUI until no errors remain	☐
10	Tell the participant that you will now turn on the fluid rendering	☐
11	Enable fluid rendering via the fluid rendering GUI	☐
12	Confirm with the participant that they are ready to start walking	☐
13	In the LokoFree control GUI, set the treadmill speed to 1 $\mathrm{km\,h^{-1}}$	☐
14	Start the stopwatch	☐
15	Once the stopwatch reaches 60 seconds, inform the participant that the trial is done, and set the treadmill speed back to 0 $\mathrm{km\,h^{-1}}$	☐
16	In the fluid rendering GUI, disable fluid rendering and data logging	☐
17	When prompted to stop the scopes and save the data, and overwrite any existing data, confirm that that is what you want.	☐
18	In the LokoFree control GUI, click stop exoskeleton	☐
19	In the treadmill GUI, click stop treadmill	☐
E	*Between Trials*	
1	Ask the participant to fill in the post-trial questions in the questionnaire	☐
2	Check that the logged data was saved correctly	☐
3	If it was the last (5th) trial of a block, ask the participant also to fill in the post-block questions of the questionnaire	☐
4	If it was the last (5th) trial of a block, shut down the exoskeleton xPC	☐
5	Once the participant is done filling in the questionnaire questions, ask them whether or not they want to take a break or want to continue to the next trial	☐
F	*Post-experiment*	
1	Thank the participant for participating in the experiment	☐
2	Store a backup of the logged data in the project drive	☐
3	Store the questionnaire in a secured cabinet	☐
4	Check that the body-weight support, the harness, the orthosis, and the treadmill show no signs of damage	☐

Appendix H: Experiment Questionnaire

Questionnaire — Version 27/11/2025

Walking through haptically rendered fluids in a lower limb exoskeleton

Participant Information

Participant ID: _____

Gender:

❍ Male ❍ Female ❍ Other: _____

Length:

_____ cm

Age:

_____

Thigh Length:

_____ cm

Weight:

_____ kg

Shank Length:

_____ cm

How often (approximately) have you walked with a leg exoskeleton before?

❍ Never ❍ Once ❍ 2-5 times ❍ 6-10 times ❍ More than 10 times

How many of those times (approximately) were with this exoskeleton specifically?

❍ I don’t know ❍ Never ❍ Once ❍ 2-5 times ❍ 6-10 times ❍ More than 10 times

Reference for the Researcher

Participant ID: _____

(Filled in by the researcher)

Exoskeleton linkage lengths

Ticks Thigh:

_____

Ticks Shank:

_____

Frontal Ticks Right:

_____

Lateral Ticks Right:

_____

Frontal Ticks Left:

_____

Lateral Ticks Left:

_____

Randomised order of the models and conditions:

Model				
Condition 1st trial				
Condition 2nd trial				
Condition 3rd trial				
Condition 4th trial				
Condition 5th trial				

Trial-specific questions: Block _____ Trial _____

Participant ID: _____

(to be filled in once after every trial)

The following questions are about the trial that just finished. Please read the questions carefully and answer them truthfully to the best of your ability. If anything is not entirely clear, please ask the researcher to clarify further.

Did you like the speed of the treadmill, or do you think a different speed would have been better?

❍ I liked the speed as it was ❍ I think faster would have been better ❍ I think slower would have been better

Perceived Forces

Based on Borg's CR-10 Rating of Perceived Exertion (RPE CR10) [36]

How strongly did you perceive the following torques and forces from the exoskeleton?

	None at all 0	Very very light ½	Very Light 1	Light 2	Mode-rate 3	Slightly strong 4	5	6	Very strong 7	8	9	Very very strong 10
Knee torques	❍	❍	❍	❍	❍	❍	❍	❍	❍	❍	❍	❍
Hip torques	❍	❍	❍	❍	❍	❍	❍	❍	❍	❍	❍	❍
Lateral pelvis forces	❍	❍	❍	❍	❍	❍	❍	❍	❍	❍	❍	❍

Realism

Adapted from the Haptic Experience Inventory (HXI) [35]

How much do you agree with the following statements?

	Strongly Dis-agree -3	Disagree -2	Somewhat Dis-agree -1	Neither Agree, Nor Dis-agree 0	Somewhat Agree 1	Agree 2	Strongly Agree 3
The haptic sensations resembled what I normally feel when walking through a real liquid	❍	❍	❍	❍	❍	❍	❍
The haptic sensations felt familiar to real life forces	❍	❍	❍	❍	❍	❍	❍
The haptic sensations closely mimicked how I would expect walking through a liquid to feel in reality	❍	❍	❍	❍	❍	❍	❍
The haptic sensations provided a true-to-life representation of a real-world liquid	❍	❍	❍	❍	❍	❍	❍

Room for notes:

End of block Questions: Block _____

Participant ID: _____

(to be filled in after every block of 5 trials)

The following questions are about the whole block of 5 trials that just finished. Please read the questions carefully and answer them truthfully to the best of your ability. If anything is not entirely clear, please ask the researcher to clarify further.

During which of the five trials of this block do you think the following fluid conditions were rendered?
(They each appeared exactly once)

No liquid rendering (Air): Trial _____ Knee-deep Water: Trial _____ Waist-deep Water: Trial _____

Waist-deep Honey: Trial _____ Waist-deep Oil: Trial _____

How confident are you in your answers?

❍ 0: Not confident at all ❍ 1: Slightly confident ❍ 2: Moderately confident ❍ 3: Very confident ❍ 4: Fully confident

How much fatigue do you currently feel in the following places?
0 = No fatigue 2 = Slight fatigue 4 = Moderate fatigue 6 = Heavy fatigue

Body Part	**Fatigue Level**						
	0	1	2	3	4	5	6
Ankles	❍	❍	❍	❍	❍	❍	❍
Lower legs	❍	❍	❍	❍	❍	❍	❍
Knees	❍	❍	❍	❍	❍	❍	❍
Thighs	❍	❍	❍	❍	❍	❍	❍
Hips	❍	❍	❍	❍	❍	❍	❍
Upper Body	❍	❍	❍	❍	❍	❍	❍

How much discomfort did you experience in the following places during the last block of trials?
Adapted from the Improved Musculoskeletal Discomfort Assessment Tool (IMDAT) [37]

Discomfort level:
0 = No Discomfort 2 = Fairly Comfortable 5 = Moderate Discomfort 8 = Very Uncomfortable 10 = Extreme Discomfort
Frequency:
0 = Never 1 = During a small subset of trials 2 = During most of the trials 3 = All the time

Body Part	**Discomfort Level**											**Frequency**			
	0	1	2	3	4	5	6	7	8	9	10	0	1	2	3
Ankles	❍	❍	❍	❍	❍	❍	❍	❍	❍	❍	❍	❍	❍	❍	❍
Lower legs	❍	❍	❍	❍	❍	❍	❍	❍	❍	❍	❍	❍	❍	❍	❍
Knees	❍	❍	❍	❍	❍	❍	❍	❍	❍	❍	❍	❍	❍	❍	❍
Thighs	❍	❍	❍	❍	❍	❍	❍	❍	❍	❍	❍	❍	❍	❍	❍
Hips	❍	❍	❍	❍	❍	❍	❍	❍	❍	❍	❍	❍	❍	❍	❍
Upper Body	❍	❍	❍	❍	❍	❍	❍	❍	❍	❍	❍	❍	❍	❍	❍

For all discomforts of level 4 or higher, can you describe the discomfort that you experienced?

Appendix I: Questionnaire Results

I.1 Realism Scores

The realism of each trial's fluid rendering was rated via four statements that each result in a score from -3 to 3. The higher each score is, the more realistic the fluid rendering was perceived to be. By summing these four scores together, as is prescribed in the haptic experience inventory [35], the total realism score is obtained. This total realism score is therefore a score from -12 to 12, with -12 the worst possible score and 12 the best possible score. The total scores for each trial of each participant are shown in table 17.

Table 17: The total realism scores for all trials of all participants. The scores can vary from -12 to 12, where a higher score represents a more realistic rendering.

	Model A – Proportional Resistance model					Model B – Aquatic Treadmill Walking model, without buoyancy and counterflow				
Fluid Condition	Air	Kd Water	Wd Water	Wd Honey	Wd Oil	Air	Kd Water	Wd Water	Wd Honey	Wd Oil
Participant 1	-4	-8	8	3	-4	-8	-4	-5	-8	1
Participant 2	4	0	3	4	4	0	0	4	4	-4
Participant 3	2	6	2	2	4	1	5	3	3	6
	Model C – Aquatic Treadmill Walking model, with buoyancy, but without counterflow					Model D – Aquatic Treadmill Walking model, with buoyancy and counterflow				
Fluid Condition	Air	Kd Water	Wd Water	Wd Honey	Wd Oil	Air	Kd Water	Wd Water	Wd Honey	Wd Oil
Participant 1						-12	-8	0	-8	-8
Participant 2	0	4	4	-4	4	0	0	-4	-8	4
Participant 3	4	5	0	2	6	8	1	3	4	3

I.2 Identification of the rendered fluids

The guesses each participant made for each trial, as well as their self-reported confidence in their guesses for each model, are listed in table 18.

Table 18: The guesses made by each participant for the rendered fluid conditions, as well as their self-reported confidence level (conf.) on a 0-4 scale with a higher score meaning a higher level of confidence. Each correct guess is shown in green and each wrong guess in red.

	Model A – Proportional Resistance model						Model B – Aquatic Treadmill Walking model, without buoyancy and counterflow					
Fluid Condition	Air	Kd Water	Wd Water	Wd Honey	Wd Oil	Conf.	Air	Kd Water	Wd Water	Wd Honey	Wd Oil	Conf.
Participant 1	Kd Water	Air	Wd Water	Wd Oil	Wd Honey	1	Air	Wd Water	Kd Water	Wd Oil	Wd Honey	0
Participant 2	Air	Wd Honey	Wd Oil	Wd Water	Kd Water	1	Wd Oil	Air	Wd Honey	Wd Water	Kd Water	3
Participant 3	Air	Kd Water	Wd Honey	Wd Oil	Wd Water	0	Air	Kd Water	Wd Oil	Wd Water	Wd Honey	1
	Model C – Aquatic Treadmill Walking model, with buoyancy, but without counterflow						Model D – Aquatic Treadmill Walking model, with buoyancy and counterflow					
Fluid Condition	Air	Kd Water	Wd Water	Wd Honey	Wd Oil	Conf.	Air	Kd Water	Wd Water	Wd Honey	Wd Oil	Conf.
Participant 1							Air	Wd Water	Kd Water	Wd Honey	Wd Oil	0
Participant 2	Air	Kd Water	Wd Water	Wd Oil	Wd Honey	2	Air	Kd Water	Wd Water	Wd Honey	Wd Oil	2
Participant 3	Wd Water	Wd Oil	Air	Kd Water	Wd Honey	1	Wd Water	Air	Wd Oil	Wd Honey	Kd Water	1

I.3 Perceived Forces

The perceived forces are rated on a 0-10 scale (Borg's CR10 rating of perceived exertion [36]) for each individual joint (Hips, knees, and pelvis) after each trial. A rating of 0 means no force perceived, while a rating of 10 is the maximum possible force. Additionally, the fatigue in those same joints and their associated body segments is rated on a 0-6 scale after each block of 5 trials, with 0 being no fatigue and 6 being heavily fatigued. These results are listed in

Table 19: Perceived force and torque ratings at the knee, hip, and pelvis from each participant for each trial of the experiment. Additionally, the reported fatigue in those joints after each block of trials is shown. For both, a higher rating reflects stronger forces/fatigue.

Participant 1												
	Model A – Proportional Resistance model						Model B – Aquatic Treadmill Walking model, without buoyancy and counterflow					
Fluid Condition	Air	Kd Water	Wd Water	Wd Honey	Wd Oil	Fatigue	Air	Kd Water	Wd Water	Wd Honey	Wd Oil	Fatigue
Knee torques	7	3	6	6	7	4	½	3	4	2	4	6
Hip torques	4	1	6	6	7	4	½	3	3	2	4	6
Pelvis Force	½	1	4	4	4	0	½	2	1	2	1	1
	Model C – Aquatic Treadmill Walking model, with buoyancy, but without counterflow						Model D – Aquatic Treadmill Walking model, with buoyancy and counterflow					
Fluid Condition	Air	Kd Water	Wd Water	Wd Honey	Wd Oil	Fatigue	Air	Kd Water	Wd Water	Wd Honey	Wd Oil	Fatigue
Knee torques							2	7	7	9	6	6
Hip torques							2	7	7	9	6	4
Pelvis Force							2	9	2	9	9	0

Participant 2												
	Model A – Proportional Resistance model						Model B – Aquatic Treadmill Walking model, without buoyancy and counterflow					
Fluid Condition	Air	Kd Water	Wd Water	Wd Honey	Wd Oil	Fatigue	Air	Kd Water	Wd Water	Wd Honey	Wd Oil	Fatigue
Knee torques	1	3	2	2	2	1	1	1	3	2	2	2
Hip torques	1	2	2	2	2	1	½	½	2	2	2	2
Pelvis Force	1	2	2	2	2	1	½	½	2	2	2	2
	Model C – Aquatic Treadmill Walking model, with buoyancy, but without counterflow						Model D – Aquatic Treadmill Walking model, with buoyancy and counterflow					
Fluid Condition	Air	Kd Water	Wd Water	Wd Honey	Wd Oil	Fatigue	Air	Kd Water	Wd Water	Wd Honey	Wd Oil	Fatigue
Knee torques	1	3	3	2	3	2	1	2	3	4	2	2
Hip torques	½	2	2	1	3	2	½	1	3	4	1	2
Pelvis Force	½	2	2	1	3	2	½	1	3	3	1	2

Participant 3												
	Model A – Proportional Resistance model						Model B – Aquatic Treadmill Walking model, without buoyancy and counterflow					
Fluid Condition	Air	Kd Water	Wd Water	Wd Honey	Wd Oil	Fatigue	Air	Kd Water	Wd Water	Wd Honey	Wd Oil	Fatigue
Knee torques	3	4	5	5	3	3	5	5	6	4	5	4
Hip torques	2	½	5	4	3	2	4	2	5	4	5	4
Pelvis Force	½	½	1	1	½	1	4	2	5	3	4	3
	Model C – Aquatic Treadmill Walking model, with buoyancy, but without counterflow						Model D – Aquatic Treadmill Walking model, with buoyancy and counterflow					
Fluid Condition	Air	Kd Water	Wd Water	Wd Honey	Wd Oil	Fatigue	Air	Kd Water	Wd Water	Wd Honey	Wd Oil	Fatigue
Knee torques	2	5	1	2	5	1	2	½	3	6	2	1
Hip torques	2	4	1	½	5	2	3	0	½	5	2	1
Pelvis Force	½	½	0	0	½	0	3	0	0	4	2	0